High-resolution Photoacoustic Spectroscopy of the Oxygen A-band

Thesis by
Elizabeth Margaret Lunny

In Partial Fulfillment of the Requirements for the
Degree of
Doctor of Philosophy

Caltech

CALIFORNIA INSTITUTE OF TECHNOLOGY
Pasadena, California

2020
Defended May 22, 2020

ACKNOWLEDGEMENTS

I would never have been able to complete this dissertation without countless people in both my academic and personal circles who have touched my life over the years.

I believe my first exposure to spectroscopy was my sophomore year of high school when one of the best educators out there, Ms. Nowak, passed around her masters thesis. I remember flipping through the book, seeing page after page of "squiggly lines" and wondering how on earth anyone could learn things from looking at these seemingly arbitrary patterns. Little did I know at the time that the incredibly solid academic foundation and enthusiasm you provided would set me on a path to knowing more than I ever thought possible about oxygen from looking at some "squiggly lines".

I continued to find some incredible educators and mentors in my professors at Providence College. I would like to thank Dr. Jack Breen for readily sharing guidance, advice, and encouragement and for continuing to check in on things during my time at Caltech. I credit Dr. Chris Laperle with preparing me for the perseverance required to complete a PhD. Your high expectations helped me to grow beyond my own expectations for myself and the experience of working with you allowed me to learn how to handle the obstacles of scientific research on a small scale, so I was ready when they came on a much larger scale in grad school.

My committee, Mitchio, Geoff, Paul, Tom and Brian were incredibly helpful during our official meetings with advice and suggestions. I appreciate your willingness to offer guidance both formally and informally throughout the process. I would like to thank Brian in a special way for being very generous with his time during our Monday meetings. I appreciate your willingness to discuss the data and teach me Labfit. Our discussions heavily impacted the way I thought about analyzing my data for this thesis and the Labfit skills made it logistically possible.

I would also like to thank everyone I collaborated with at NIST during my two visits there. Thanks to Jimmy Radney and Chris Zangmeister for teaching me about aerosols and aerosol spectroscopy. I would also like to thank Joe Hodges, Dave Long and Erin Adkins for the opportunity to work with them on the cavity ring-down A-band measurements as well as for many helpful conversations about the photoacoustic data.

I would like to thank Mitchio for the countless hours of guidance and support he has provided during my graduate career. You were always ready to provide helpful insights about the scientific problem at hand, but also had a special ability to notice the times when I was frustrated and provided meaningful words of encouragement when they were most needed. I will miss working with you.

I feel lucky to have worked with so many phenomenal people in the Okumura Group during my time in grad school. From journal clubs, to group lunches, to office chats, to camping trips, I have countless great memories because of the wonderful people these moments were shared with. Thanks Thinh, Leah, Linhan, Laura, Aileen, Matt, Joey, Greg, Doug, Hannah, Leah, Wen, Luis, Damien, Fred, Matt, Tzu-Ling and Ofir.

So many colleagues became good friends. Thanks to Thinh Bui for helping me to get started in the quiet room and always having a great joke ready for every occasion. Thanks to Leah Dodson for being the closest thing I have had to an older sister. I appreciate you tolerating my Christmas-themed shenanigans, always being willing to listen, give advice, laugh and provide "stress relief". Thanks to Linhan Shen for pushing me outside my comfort zone, for forcing me to go on adventures that I was hesitant about but then loved, for introducing me to new foods and for inserting yourself into my family ensuring our adventures will certainly continue. I think all of the "Lunnies" agree that we couldn't find a better addition. Thanks to Aileen Oyama Hui for being my favorite cooking companion, the first to let me know where the free food is, and a super supportive friend at every moment of this journey. Thanks to Matt Smarte for being my favorite person on earth to "fight" with (even though its really not a fair match since I'm always right). Sharing pretty much every moment of grad school with you certainly had its ups and downs, but I am incredibly thankful for having a buddy along the way- we lifted each other up, challenged each other, made lots of memories and, through friendship, grew as scientists and as people. Thanks to Joey Messinger for always being ready to discuss baking shows or life in general. Thanks to Greg Jones for many memorable office chats. Thanks to Doug Ober for being a constant source of entertainment and for always being willing to help out. Thanks to Hannah Szentkuti for your positive attitude and the fun atmosphere you bring to all group events.

I also managed to squeeze in a few friends outside the Okumura Group. Thanks to Crystal Chu for the many boba chats, Target trips and adventurous culinary experiences. Grad school wouldn't have been the same without you (and Yali!). Thanks to Katerina Korch for the many memories we made as roommates-from patio time to tea time to couch time, I have many great memories from all of the time. Thanks to Hannah Allen, the best officemate I could have hoped for. I can't even imagine how many evenings were spent chatting about life, commiserating about "negative progress" that day or analyzing humanity over the last five years, but it was always a great way to end the day. You brought so much needed joy to life in the subbasement.

The last two years of my grad school career were made infinitely more enjoyable through the unexpected, but treasured second generation of grad school friends resulting from my aversion to "nerdy" movies. During some of the most stressful times, it was always nice to take a break for a movie marathon and a potluck with Stephanie, Jorge, Joaquin, Joanie, Tim and Maria. Thank you guys for the cultural enlightenment, great cooking, fellowship and many memories. And a special thanks to Stephanie, my favorite person to wander the streets of Pasadena with. Whether we were sharing the up and downs of grad school, discussing the latest podcasts or exchanging recipes, our chats were always filled with laughter that brightened many days.

I would like to thank my extended family for the immense love and support. There are too many to list by name, but I always looked forward to going home twice a year and being welcomed with open arms, like I had only been gone for a week. I appreciate all of the text messages, phone calls and Snapchats from the younger ones and the cards, baked goods and phone calls from the older ones. I think you kept the USPS in business for the last seven years with all of the greeting cards I got for every imaginable holiday. It was always nice to see a bright colored envelope in my mailbox on my way home from a long day-and they kept coming even when I was horrible at responding. Thanks family, love you all!

Finally, I would like to acknowledge my immediate family. I would never have been able to complete this thesis without your constant love and support throughout my whole life. I would like to thank my dad for instilling a strong work ethic and sense of integrity through his example. I would like to thank my mom for instilling a sense of curiosity through the many library trips, museum visits and other crazy adventures of my childhood. And Katharine, I think there are few people who have the privilege of sharing this many life experiences with another human being. From building forts to racing bikes to going to conferences together to commiserating over broken lasers, there is no one I would rather do it with than you, bud! Can't wait to see what the next chapter holds for us as we head back to Massachusetts!

ABSTRACT

There have been many advances in recent years in remote sensing and ground-based measurement technologies utilizing optical detection to identify and quantify species in the atmosphere. Many of these instruments record high signal-to-noise spectra requiring sophisticated spectral modeling beyond the Voigt profile. In order to properly quantify the higher order spectral effects, high-resolution laboratory data measuring samples of known composition under carefully controlled conditions are required.

The oxygen A-band is used in a number of atmospheric composition measurements due to the uniform, well-known concentration of oxygen throughout the atmosphere. Previous laboratory A-band measurements using cavity ring-down spectroscopy and Fourier transform spectroscopy have greatly improved the understanding of spectral parameters. However, current spectral models are insufficient to fit some high quality remote sensing data, such as the OCO missions. The largest spectroscopic uncertainties in modeling result from characterization of line mixing and collision-induced absorption. These collisional effects, resulting in small absorption changes in the baseline and wings, which become more prominent at elevated pressures can be accurately measured with photoacoustic spectroscopy, a background free measurement with a large dynamic range producing high signal-to-noise spectra.

A novel high-resolution photoacoustic spectrometer was designed and constructed to improve the understanding of A-band spectral parameters to meet the OCO mission goals. The spectrometer is capable of measuring both the P and R-branches of the A-band up to J'=28 with a signal-to-noise ratio of 30,000 for pressures of 50-4,000 Torr. A temperature control system was also implemented to allow for measurements over the range of atmospherically relevant temperatures.

Results from spectral fitting of data from the newly developed spectrometer provide the most accurate A-band pressure shift coefficients for both oxygen and air measured to date. The data also indicates the importance of lineshape profile choice for resonant absorption in order to accurately characterize line mixing and collision-induced absorption; the speed-dependent Nelkin-Ghatak profile is required for the current data set. Finally, preliminary fitting of line mixing and collision-induced absorption suggests the photoacoustic data achieves the required sensitivity to provide improved understanding of line mixing and collision-induced absorption based on fundamental physical principles.

TABLE OF CONTENTS

LIST OF ILLUSTRATIONS

LIST OF TABLES

Chapter 1

INTRODUCTION

Abstract

Anthropogenic carbon emissions result in elevated atmospheric carbon dioxide (CO_2) levels which result in a net increase in global temperatures. It is unclear how the Earth will respond to further increases in carbon dioxide emissions. The OCO missions are designed to measure global sources and sinks of carbon dioxide with unprecedented spatial and temporal resolution. These instruments utilize absorption of reflected sunlight to quantify the dry air mole fraction of CO_2. The oxygen A-band is used to determine solar pathlength; any errors resulting from oxygen spectroscopic models propagate through to retrieved column CO_2 measurements. Therefore, high-resolution laboratory studies of the oxygen A-band are critical to meet the mission needs.

1.1 Atmospheric Carbon Dioxide Measurements

Multiple independently produced data sets have concluded that the Earth's average annual temperature has increased $0.97°C$ since 1880 [1]. Increased global temperatures lead to rising sea levels, altered precipitation patterns and changes in the frequency of extreme weather. These consequences present a number of threats to society including property destruction, decreased crop production and human health issues.

These increasing annual temperatures are due to the current radiative imbalance of Earth; more energy enters the atmosphere than is released resulting in heating. Most of this heat is absorbed by oceans (93%), followed by melting ice (3%) and continental warming (3%) with the remaining heat being absorbed by the atmosphere (1%) [1].

One of the significant sources of this radiative imbalance is the ever-growing concentration of greenhouse gases in the atmosphere. Gases which absorb at outgoing long-wave radiation wavelengths ($> 3\mu$m) trap radiation resulting in a net increase in thermal energy of the Earth and its atmosphere. As the most abundant anthropogenic greenhouse gas, carbon dioxide (CO_2) is the most significant contributor to total radiative forcing. Ice core data reveals that current atmospheric concentrations of carbon dioxide (CO_2) are the highest in the last 800,000 years [2]. Current CO_2 concentrations have not only reached the highest concentrations for available data, but levels are also increasing at unprecedented rates. Figure 1.1a shows the historic atmospheric carbon dioxide concentrations and $^{13}C/^{12}C$ stable isotope ratios from ice core data for the last 600 years. There is a clear, sudden onset of exponential growth beginning around 1750 with the dawn of the industrial revolution. This growth in atmospheric carbon dioxide levels is accompanied by a trend toward more negative stable isotope ratios which are indicative of carbon dioxide originating from the burning of fossil fuels.

Fossil fuel combustion disrupts the natural carbon cycle of Earth. The burning of fossil fuels by humans as an energy source releases the carbon stored away in these long-term sinks into the active carbon cycle disrupting the natural equilibrium. Figure 1.1b shows that the major anthropogenic sources of CO_2 are fossil fuel burning and cement while changes in land use also produce CO_2. However, natural environmental sinks are able to partially offset the anthropogenically produced CO_2. Oceans and the biosphere absorb about half of the anthropogenic CO_2 each year, with the remaining $\sim$ 17 gigatons/year accumulating in the atmosphere [3].

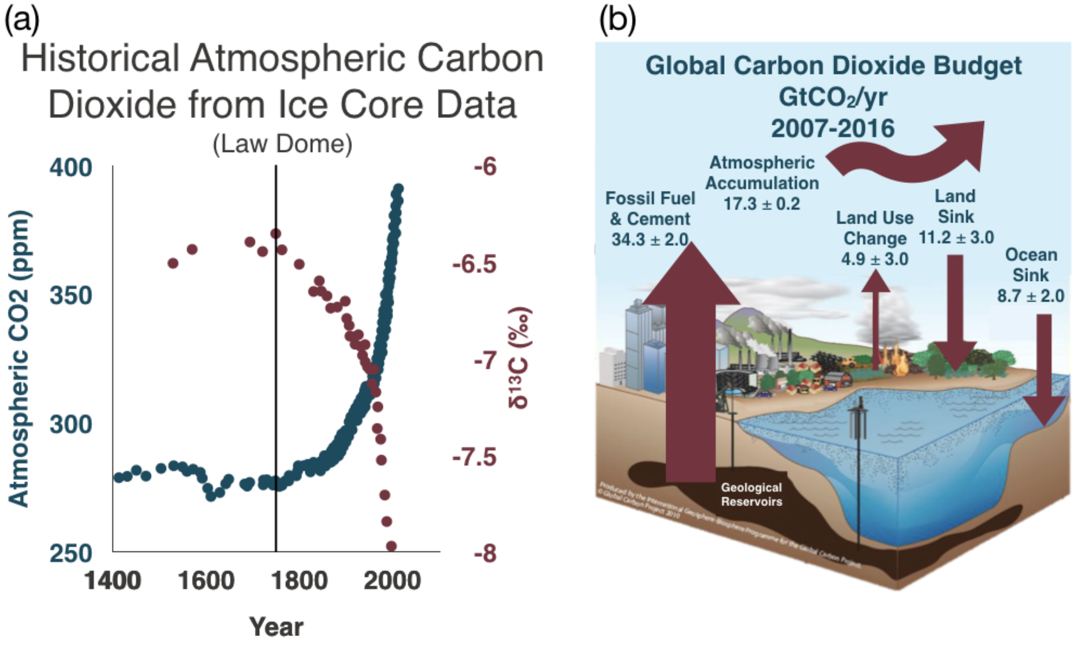

Figure 1.1: (a)Historic atmospheric carbon dioxide concentrations and the $^{13}C/^{12}C$ stable isotope ratios from ice core data demonstrating drastic changes after the industrial revolution due to increasing use of fossil fuels on a global scale. From [2] (b) Carbon dioxide source and sink information from 2007-2016. From [4]

The annual atmospheric accumulation of CO_2 leads to increasing concentrations of CO_2 in the atmosphere over time which have been accurately measured at the Mauna Loa Observatory in Hawaii [5]. These measurements demonstrate the seasonal variability of atmospheric carbon dioxide levels corresponding to growing seasons in addition to the overall year to year increase. There is a clear correlation between increasing CO_2 concentrations in the atmosphere and elevated anthropogenic CO_2 production. While on average about 50% of the anthropogenically produced CO_2 accumulates in the atmosphere with the remainder absorbed by the oceans and biosphere, the fraction can change significantly from year to year. As Figure 1.1b shows, the fraction of CO_2 accumulating in the atmosphere in 1987 was nearly 80% while just 5 years later, in 1992 the accumulated fraction of CO_2 was only about 20% [4]. This observation leads to a number of interesting scientific questions including: What causes this variation from year to year? How will the CO_2 sinks respond if the atmospheric CO_2 concentrations continue to grow at an increasing rate?

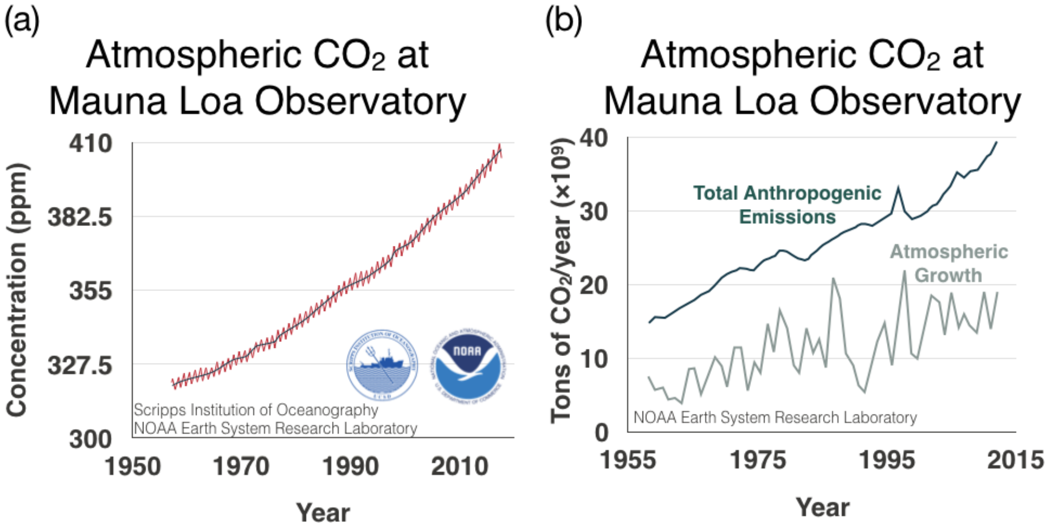

Figure 1.2: (a) Mauna Loa observations of atmospheric CO_2 concentrations demonstrating seasonal variability and an increasing rate of accumulation. From [5] (b) Anthropogenic emissions and atmospheric accumulation of CO_2.

From [4]

1.2 OCO Missions

The Orbiting Carbon Observatory missions (OCO-2 and OCO-3) seek to address these important questions by monitoring sources and sinks of CO_2 on a global scale with unprecedented spatial and temporal resolution [6, 7, 8].

OCO-2 is a NASA satellite successfully launched on July 2, 2014 which measures the column-integrated CO_2 dry air mole fraction. It is in the A-train, a near sun synchronous orbit, with a number of other satellites which are also measuring various aspects of climate change. The satellite achieves near global coverage on a 16-day cycle which alternates between 2 viewing modes: nadir and glint. OCO-2 collects approximately 9,000 frames per orbit. Each frame consists of eight spectra which measure a surface footprint of about 3 km^2 resulting in over 72,000 soundings on the sunlit side of the orbit.

OCO-3 is a NASA instrument mounted on the International Space Station which was partially constructed with spare parts from the OCO-2 mission. It was launched on May 4, 2019 and is also designed to measure global sources and sinks of carbon dioxide. The observations cover 52 degrees North to 52 degrees South latitudes, but the orbit passes over an area at different times of day, so unlike the OCO-2 satellite, OCO-3 is capable of measuring carbon dioxide concentration patterns over the course of a single day at different locations around the globe. In addition, a pointed mirror assembly allows for rapidly alternating viewing modes and a "snapshot" mode where an 80×80 km^2 area can be measured in a single pass to target regions of interest.

Both missions seek to determine the location and seasonal variability of CO_2 sources and sinks by applying computer-based assimilation models to the retrieved the column-integrated CO_2 dry air mole fraction. While there are a number of satellites monitoring total CO_2 concentrations, identification of sources and sinks requires measurements of small changes in CO_2 concentrations; the goal of both missions is to measure dry air mole fractions of CO_2 with 1 ppm (0.25%) precision.

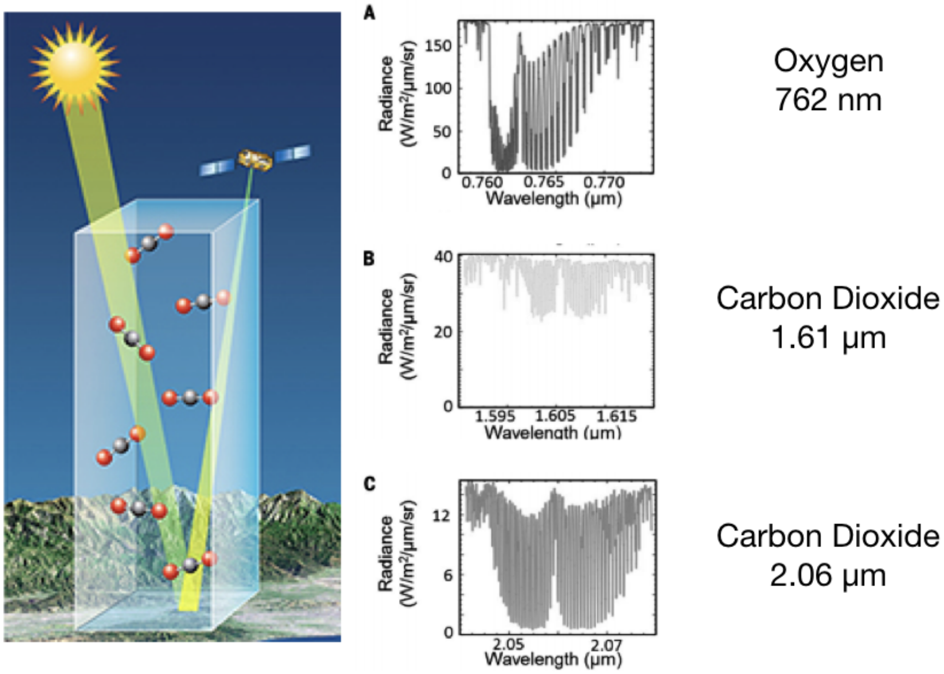

Figure 1.3: (a) OCO-2 satellite schematic of reflected sunlight measurement and (b) Spectroscopic regions covered by spectrometers on the instruments for the OCO missions

Carbon dioxide dry air mole fractions are measured with three high-resolution spectrometers on both OCO-2 and OCO-3. These instruments are designed to utilize reflected solar radiation in order to measure the O_2 A-band and two CO_2 bands, 1.61μm and 2.06μm (shown in Figure 1.2). Near infrared bands were chosen which display high sensitivity in measurements near the surface, where most CO_2 sources and sinks are located. The two CO_2 bands provide independent CO_2 retrieval paths while the oxygen A-band is used to determine solar pathlength.

The resulting maps are shown in Figure 1.6. The measurements are able to resolve CO_2 concentrations on the part per million scale. In general, concentrations are higher in the northern hemisphere where the majority of industrialized countries are. In addition, seasonal variability can be observed. In March (top) the concentrations are lower in the southern hemisphere compared to June because it is the growing season. In contrast, CO_2 concentrations are lower in June compared to March in the northern hemisphere due to the increased biomass at that time. The satellite achieves global coverage, but it can also measure variation on local scales. Figure 1.6b shows two passes over the Los Angeles area. The seasonal variability is easily resolved, but in addition, the elevated CO_2 concentrations are observed in a more urban location (Pasadena) compared to the desert (Edwards Air Force Base). The satellite measurements also show good agreement with the ground based TCCON CO_2 sensing network.

Currently, the most significant spectroscopic uncertainties leading to errors in the retrieved dry air mole fraction of CO_2 are line mixing (LM) and collision-induced absorption (CIA) in the oxygen A-band. These collisional phenomena result in small changes to the spectra in the wings of absorption lines where the satellite is most sensitive to absorption due to the long pathlength of twice the atmosphere. Therefore, A-band spectral parameters must be accurately characterized by laboratory spectroscopic efforts under well controlled conditions in order to improve the accuracy of retrieved column CO_2 mole fractions from OCO-2 and OCO-3 data sets.

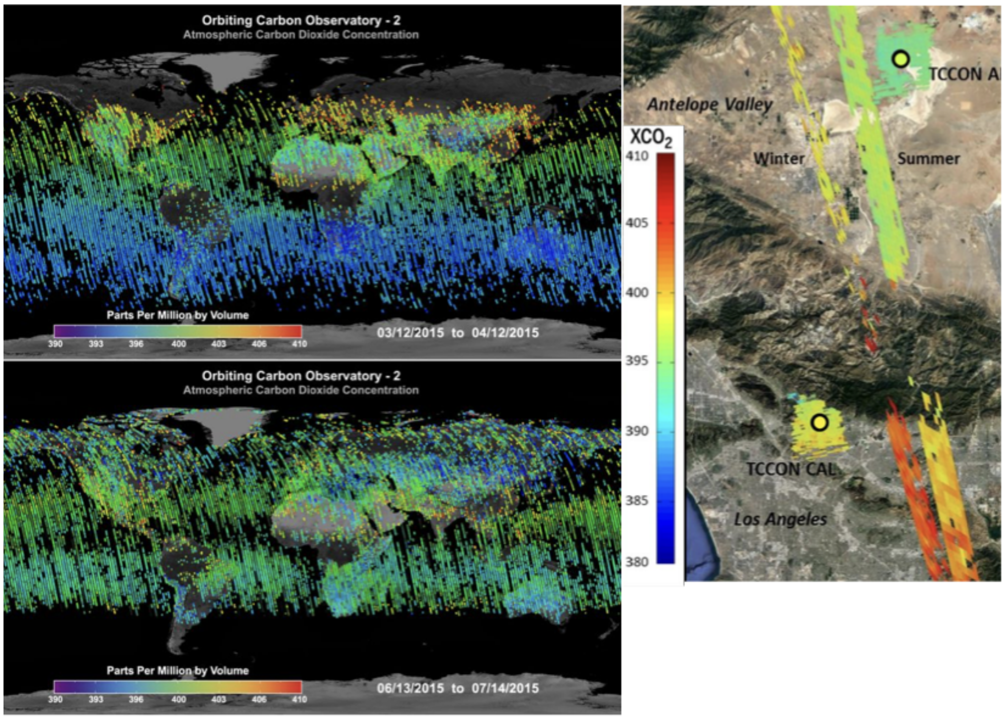

Figure 1.4: (a) Global maps of CO_2 dry air mole fractions in winter (top) and summer (bottom) (b) CO_2 map over the Los Angeles area from [9]

1.3 A-band Spectroscopy

Absorption measurements of the O_2 A-band have been used in a number of both satellite and ground based atmospheric composition measurements for purposes such as measuring pressure and temperature vertical profiles, determining surface pressure or quantifying the pathlength of solar radiation. OCO-2 uses the O_2 A-band in order to measure the solar radiation pathlength, accounting for the presence of aerosols or clouds and to determine total atmospheric pressure.

The oxygen A-band at 760 nm has traditionally been used as a reference for atmospheric composition measurements due to the precisely known, uniform distribution of molecular oxygen throughout the atmosphere and the spectral isolation of the band. The transition is quantum mechanically triply forbidden which allows for the measurement of unsaturated high-J rovibronic lines after two passes through the atmosphere.

While the A-band transition, $b^1\Sigma_g^+ \leftarrow X^3\Sigma_g^-(0,0)$, is triply forbidden by electric dipole selection rules, magnetic dipole and electric quadrupole transitions have been observed although they are 10^7 and 10^{12} times weaker than typical electric dipole transitions, respectively.

Molecular oxygen ($^{16}O_2$) is most closely approximated by Hund's case b in which spin-orbit coupling is weak. Under these circumstances, the rotational levels are described by quantum numbers S, N = R + L and J = N + S where S is the spin angular momentum, N is the rotational angular momentum (the sum of R, the nuclear rotation angular momentum and L, the orbital angular momentum) and J is the total angular momentum. The $X^3\Sigma_g^-$ ground state is split into three energy levels ($\mathrm{J} = \mathrm{N} - 1, \mathrm{N}, \mathrm{N} + 1$) due to spin-rotation coupling. The singlet nature of the $b^1\Sigma_g^+$ excited state results in one energy level for each N value. For, $^{16}O_2$ ground state rotational angular momentum must be odd and the excited state rotational angular momentum must be even due to spin statistics. As shown in Figure 1.3a, the magnetic dipole selection rule of δJ = 0, 1 results in a series of doublets in both the P and R branches described by δNδJ as shown in Figure 1.3b. The spacing between P-branch doublets (PP and PQ branches) increases with increasing J while the spacing between R-branch doublets (RR and RQ branches) decreases with increasing J resulting in a bandhead around 13,165 cm^{-1}.

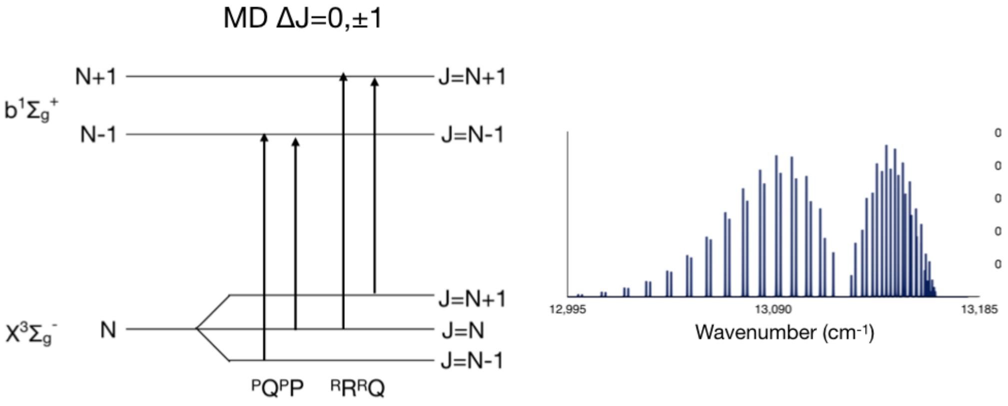

Figure 1.5: (a) Oxygen energy levels and allowed magnetic dipole transitions (b) A-band spectrum

In contrast to previous missions, which measured a single rovibronic line, OCO-2 measures full bands. This leads to a number of challenges including precise, extensive knowledge of parameters associated with the spectral shape of individual lines and a quantitative understanding of physical processes which simultaneously impact multiple transitions. These processes include line mixing, which involves a population transfer from one transition to another and collision-induced absorption which results in a broad weak absorption underlying the entire band.

Technical advances in remote sensing instrumentation have allowed for a new generation of high-resolution spectroscopic measurements with signal to noise that requires more sophisticated lineshape models to describe the physics captured in the data.

An isolated spectral line is described by the transition frequency, integrated intensity and a lineshape profile. The transition frequency is primarily determined by the spacing of energy levels intrinsic to the molecule of interest; however, small yet significant perturbations to the transition frequency can result from collisional effects. The advancement of spectroscopic techniques have greatly improved the ability to measure integrated intensities of isolated spectral lines with the largest error often coming from the composition of the gas sample. The choice of lineshape profile can significantly impact retrieved parameters and must be chosen carefully to align with the available data (SNR and molecule identity). Lineshapes will be further discussed in Section 1.4.

Collisional effects can perturb the isolated absorption lines arising from the interaction of a single analyte molecule with radiation. Line mixing, referring to the collisional transfer of energy between closely spaced energy levels, results in the transfer of intensity between absorption lines. Collision-induced absorption arises from the short-lived dipoles induced during a collision which can allow for the absorption of radiation. While line-mixing rearranges intensity, collision-induced absorption is additional to the dipole moment squared band intensity. It scales as number density squared as a bimolecular collision. Line mixing will be discussed further in Section 1.5 and collision-induced absorption will be discussed in Section 1.6.

1.4 Resonant Lineshape

Isolated absorption lines can be defined by three quantities: the transition frequency, the integrated intensity and the lineshape profile. The absorption coefficient (α) at any frequency (ν) can be defined as:

$$\alpha(\nu) = \mathrm{ncS(T)f}(\nu - \nu_0)$$

where n is the number density of the absorbing species, c is the speed of light, S(T) is the temperature dependent line intensity and $f(\nu - \nu_0)$ is the lineshape function centered at the frequency ν_0. The lineshape profile is described by parameters accounting for physical phenomena briefly described below.

Lifetime Broadening

All spectroscopically observed transitions have an intrinsic linewidth due to the Heisenberg time-energy uncertainty principle. The lifetime associated with the spontaneous emission of radiation necessarily leads to a finite observed linewidth. This phenomena can be described with a Lorentzian profile, although it is often negligible compared to other broadening processes and can be neglected in lineshape calculations.

Doppler Broadening

Translation of molecules in the laboratory frame gives rise to shifts in the incident radiation in the molecular frame due to the Doppler effect. This phenomenon is described by a Gaussian function:

$$F_D(\nu - \nu_0) = \sqrt{\frac{ln(2)}{\pi}}\frac{1}{\Gamma_D}\exp -ln(2)(\frac{\nu - \nu_0}{\Gamma_D})^2$$

with a Doppler half width of:

$$\Gamma_D = \sqrt{\frac{2ln(2)kT}{mc^2}}\nu_0$$

where k is the Boltzmann constant, T is the temperature of the gas, m is the molecular mass of the absorbing species and c is the speed of light. For A-band transitions, Γ_D varies slightly across the band, but is typically about 0.4 GHz or $1.4 \times 10^{-2} cm^{-1}$.

Pressure Broadening

Molecular collisions of the radiating molecule with a perturber molecule lead to energy transfer processes which shorten the lifetime of both the initial and final state. This results in both a broadening of the lineshape and a shifting of the observed line center. These phenomena are described by a Lorentzian profile:

$$F_L(\nu - \nu_0) = \frac{1}{\pi} \frac{\Gamma_0}{(\nu - \nu_0 - \Delta)^2 + \Gamma_0^2}$$

where Γ_0 is the pressure-broadened half width and Δ is the pressure-induced shift.

Dicke Narrowing

When the mean time between collisions is short compared to transition time, or in other words, the mean free path of a molecule is much smaller than the wavelength of absorbed radiation, collisional events during an absorption event result in an averaging over Doppler states and thus a narrowing of the Doppler profile. This can be modeled with either a hard collision model, where there is no memory of the pre-collision velocity, or a soft collision model in which several collisions are required for velocity changes. This phenomenon is described by the Dicke profile:

$$F_{Dk}(\nu - \nu_0) = \frac{1}{\pi} \frac{\Gamma + k^2 D_0/P}{(\nu - \nu_0 - \Delta)^2 + (\Gamma + k^2 D_0/P)^2}$$

Speed Dependence

In the mechanisms considered above, the velocity and rovibrational relaxation are assumed to be independent; however, they can be coupled inducing an asymmetry to the lineshape profile. In this case, the velocity distribution cannot be considered symmetric around an average value and becomes asymmetric. Speed dependence impacts both the width and shift of spectral lines, but in the case of the oxygen A-band, in previous studies and in the current work, the speed-dependent shift is considered negligible.

Lineshape Profiles

The lineshape parameters that define various lineshape profiles are summarized in Table 1.1.

Doppler Profile: accounts for Doppler broadening

Lorentz Profile: accounts for pressure broadening and pressure-induced shifts

Voigt Profile: accounts for Doppler broadening, pressure broadening and pressure-induced shifts

Galatry Profile: accounts for Doppler broadening, pressure broadening, pressure-induced shifts and Dicke narrowing with soft collision model

Nelkin-Ghatak Profile: accounts for Doppler broadening, pressure broadening, pressure-induced shifts and Dicke narrowing with hard collision model

Speed-dependent Voigt Profile: accounts for Doppler broadening, pressure broadening, pressure-induced shifts and speed-dependence

Speed-dependent Galatry Profile: accounts for Doppler broadening, pressure broadening, pressure-induced shifts, Dicke narrowing with soft collision model and speed-dependence

Speed-dependent Nelkin-Ghatak Profile: accounts for Doppler broadening, pressure broadening, pressure-induced shifts, Dicke narrowing with hard collision model and speed-dependence

Hartmann-Tran Profile: accounts for Doppler broadening, pressure broadening, pressure-induced shifts, Dicke narrowing with hard collision model and speed-dependence with correlations between velocity and rotational state changes

Lineshape Parameters	
Doppler (DP)	Γ_D
Lorentz (LP)	Γ_0, Δ_0
Voigt (VP)	$\Gamma_D, \Gamma_0, \Delta_0$
Galatry (GP)	$\Gamma_D, \Gamma_0, \Delta_0, \nu_{VC}$
Nelkin-Ghatak (NGP)	$\Gamma_D, \Gamma_0, \Delta_0, \nu_{VC}$
Speed-dependent Voigt (SDVP)	$\Gamma_D, \Gamma_0, \Delta_0, \Gamma_2, \Delta_2$
Speed-dependent Galatry (SDGP)	$\Gamma_D, \Gamma_0, \Delta_0, \Gamma_2, \Delta_2, \nu_{VC}$
Speed-dependent Nelkin-Ghatak (SDNGP)	$\Gamma_D, \Gamma_0, \Delta_0, \Gamma_2, \Delta_2, \nu_{VC}$
Hartmann-Tran (HTP)	$\Gamma_D, \Gamma_0, \Delta_0, \Gamma_2, \Delta_2, \nu_{VC}, \eta$

Table 1.1: Lineshape model parameters. Γ_D is the Doppler HWHM, Γ_0 is the Lorentzian HWHM, Δ_0 is the pressure shift, Γ_2, Δ_2, ν_{VC}, γ_{KS}, η

1.5 Line Mixing

The lineshape modeling discussion in the above section assumes isolated transitions; however, when the spacing between optical transitions is the same order of magnitude as the pressure broadened width, collisional population exchange can result in intensity exchange between individual absorption lines known as line mixing. A collision between two molecules can result in population transfer followed by photon absorption and a second collisional transfer. In this case, the initial and final states of the molecules are unchanged, but the energy of the absorbed photon differs. This results in an intensity exchange between the absorption lines. Due to detail balance relationships, there is a net transfer from stronger lines to weaker ones impacting the wings and peaks of lines most significantly. Figure 1.6 shows modeled pure oxygen 2900 Torr spectra neglecting line mixing and with the inclusion of line mixing. The bottom panel shows the difference between the line mixing and no line mixing models. Under these conditions, neglecting line mixing would result in residuals on the order of 1% Line mixing increases at higher pressure due to the collisional nature of the effect. Line mixing and theoretical treatments of it will be discussed in detail in Chapter 4.

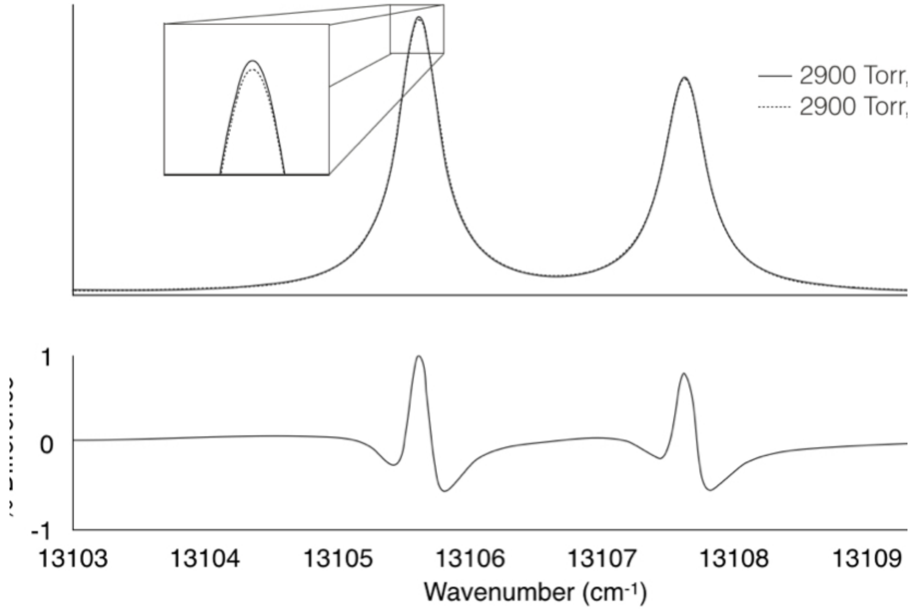

Figure 1.6: (a) Modeled 2900 Torr pure oxygen lineshapes with and without line mixing and (b) difference between line mixing and no line mixing

1.6 Collision-Induced Absorption

In addition to the resonant absorption which is proportional to the number density and square of the dipole moment, collisionally induced dipoles can lead to additional absorption. The intensity of collision-induced absorption scales with number density squared due to the bimolecular nature of the collision. These collisions are very short lived, on the order of 10^{-13} leading to a broad absorption feature under the resonant absorption. In the A-band, the collision-induced absorption is very weak compared to the resonant lines. Figure 1.7 shows modeled spectra for 2900 Torr of pure oxygen with and without collision-induced absorption in the region of the strongest peaks. This spectral region also corresponds to the part with the strongest collision-induced absorption; however even at 2900 Torr, it is only about 0.25% of the peak resonant absorption. The shape of the feature is impacted by the identity of the perturber and will be discussed in detail in Chapter 4.

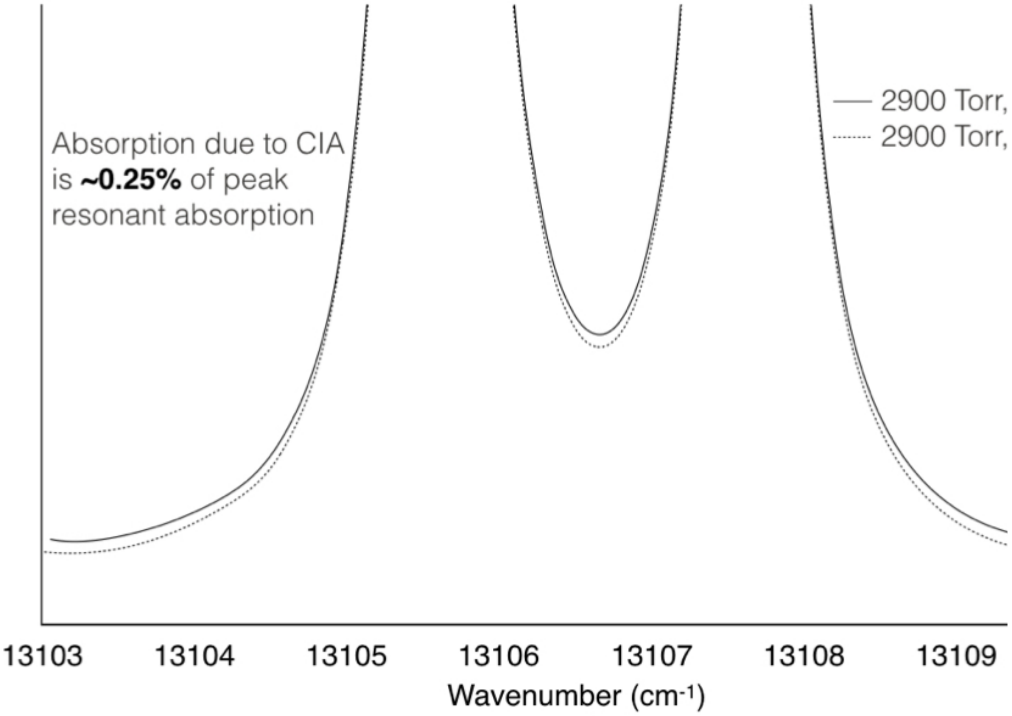

Figure 1.7: Modeled spectra with and without collision-induced absorption, 2900 Torr pure oxygen

References

[1] *NOAA National Centers for Environmental Information, State of the Climate: Global Climate Report for Annual 2019, published online January 2020, retrieved on May 1, 2020 from https://www.ncdc.noaa.gov/sotc/global/201913*.

[2] M. Rubino et al. “A revised 1000 year atmospheric 13C-CO2 record from Law Dome and South Pole, Antarctica”. In: *Journal of Geophysical Research: Atmospheres* 118.15 (2013), pp. 8482–8499. ISSN: 2169-8996. DOI: `10.1002/jgrd.50668`.

[3] P. Friedlingstein et al. “Global Carbon Budget 2019”. In: *Earth System Science Data* 11.4 (Dec. 4, 2019). Publisher: Copernicus GmbH, pp. 1783–1838. ISSN: 1866-3508. DOI: `https://doi.org/10.5194/essd-11-1783-2019`.

[4] NOAA US Department of Commerce. *ESRL Global Monitoring Laboratory - Research Areas*. Library Catalog: www.esrl.noaa.gov. URL: `https://www.esrl.noaa.gov/gmd/about/theme1.html`.

[5] R.F. Keeling and Charles D. Keeling. *Atmospheric Monthly In Situ CO2 Data - Mauna Loa Observatory, Hawaii*. 2017.

[6] C. E. Miller et al. “Spectroscopic challenges for high accuracy retrievals of atmospheric CO2 and the Orbiting Carbon Observatory (OCO) experiment”. In: *Comptes Rendus Physique*. Molecular spectroscopy and planetary atmospheres 6.8 (Oct. 1, 2005), pp. 876–887. ISSN: 1631-0705. DOI: `10.1016/j.crhy.2005.09.005`.

[7] C. E. Miller et al. “Precision requirements for space-based data: REQUIREMENTS FOR SPACE-BASED”. In: *Journal of Geophysical Research: Atmospheres* 112 (D10 May 27, 2007). ISSN: 01480227. DOI: `10.1029/2006JD007659`.

[8] A. Eldering et al. “The OCO-3 mission: measurement objectives and expected performance based on 1 year of simulated data”. In: *Atmospheric Measurement Techniques* 12.4 (Apr. 15, 2019). Publisher: Copernicus GmbH, pp. 2341–2370. ISSN: 1867-1381. DOI: `https://doi.org/10.5194/amt-12-2341-2019`.

[9] A. Eldering et al. “The Orbiting Carbon Observatory-2 early science investigations of regional carbon dioxide fluxes”. In: *Science* 358.6360 (Oct. 13, 2017). ISSN: 0036-8075, 1095-9203. DOI: `10.1126/science.aam5745`.

Chapter 2

HIGH-RESOLUTION, BROADBAND, LOW TEMPERATURE PHOTOACOUSTIC SPECTROMETER

2.1 Abstract

A broadband photoacoustic spectrometer was developed in order to quantify line mixing and collision-induced absorption in the oxygen A-band to meet the needs of the OCO missions. The spectral coverage includes 12,995-13,190 cm^{-1} including J'<28 for the P-branch and extending beyond the bandhead of the R-branch. An automated scanning program allows for collection of a single spectrum of about 15,000 data points in 21 hours, a reasonable timescale for maintaining sample conditions (pressure, temperature, etc.). The resulting spectra demonstrate signal-to-noise ratios in excess of 30,000 for the 21 hour scan time. In contrast to spectroscopic methods relying on direct optical detection, the dynamic range is limited by the pressure rating of the cell; unsaturated lineshapes can be measured over a wide range: 50-4,000 Torr. The extension of the measurable range beyond atmospherically relevant pressures is important to exaggerate line mixing and collision-induced absorption and decouple the the two by constraining models to known pressure dependencies over a wider range.

2.2 Introduction

The photoacoustic effect was first observed by Alexander Graham Bell in the 1880s [1]. Bell observed sound when a beam of sunlight passing through a rotating slotted disk was reflected off of a sample of selenium and later other materials as well. He correctly hypothesized that the sound was produced from heat generated by absorption of light by the material of interest. In the next few years, John Tyndall [2] and Wilhelm Rontgen extended the principle to the measure of heat generated by liquids and gases excited with a modulated light source. However, these experiments were all conducted with sunlight as the light source and the human ear as the sound detector. Practical applications remained limited until advancements in light sources and signal transducers made quantitative measurements feasible. The first quantitative analysis was achieved by Viengerov in the 1930s using a Nernst glower and a microphone to detect carbon dioxide [3]. Photoacoustic spectroscopy became popular in the 1970s with enhanced capabilities with the use of lasers.

The technique has become wide spread with hundreds of papers published each year utilizing photoacoustic spectroscopy for the past several decades. Many innovative detection methods to enhance the sensitivity have been explored including cantilever enhanced photoacoustic spectroscopy[4], cavity enhanced photoacoustic spectroscopy [5] and quartz enhanced photoacoustic spectroscopy [6]. In addition, a photoacoustic spectrometer coupled to a frequency comb was recently developed [7] allowing for rapid broadband measurements.

These technical advances have allowed for numerous applications including trace gas detection and quantification, kinetics studies, measurement of aerosol absorption properties and characterization of liquids/solids. Trace gas applications are extensive but include indoor air quality, greenhouse gas monitoring[8] and breath analysis for medical diagnosis. Liquid and solid applications include water ice phase transitions and food quality evaluation [9].

While many of the techniques mentioned above involve measuring the presence of a specific analyte or identity of a sample, high-resolution photoacoustic spectroscopy has also been implemented for lineshape studies. For example, Gillis [10] designed a photoacoustic spectrometer for the oxygen A-band for quantitative measurements which agreed with the modeled response at the 1% level. High-resolution photoacoustic spectroscopy has also been utilized to monitor carbon dioxide concentrations with high accuracy [8]. However, both of these experiments were done for a single rovibrational peak. To our knowledge, the current work is the first application of high-resolution photoacoustic spectroscopy over a wide spectral range.

2.3 Measurement Principles

A photoacoustic signal is generated from the periodic pressure wave produced from nonradiative decay of an analyte optically excited by a modulated light source. The power of the technique lies in the fact that the amplitude of the observed pressure wave, normalized to the power is directly proportional to the absorption coefficient:

$$S(\lambda) = \frac{p}{W} = C_{cell}R(\omega\tau)\alpha(\lambda)$$

where S is the photoacoustic signal defined as the amplitude of the pressure wave measured by the microphone (p) divided by the peak-to-peak laser power (W). This quantity is equal to the product of the cell constant (C_{cell}), the relaxation response function ($R(\omega\tau)$) and the absorption coefficient (α).

The cell constant is dependent only on the geometry of the photoacoustic cell and the properties of the sample gas. It is defined as:

$$C_{S1} = \frac{\gamma - 1}{\beta_P T} \times \frac{Q_{S1} G_{S1} L}{2\pi f_{S1} V}$$

for the lowest order mode of the cell design used in this work. γ is the specific heat ratio, $\beta - P$ is the volume expansivity, T is the temperature, Q_{S1} is the quality factor of the resonant mode, G_{S1} is the overlap integral, L is the length of the cell, f_{S1} is the frequency of the lowest order mode. None of these quantities depend on the optical frequency, so the cell constant is not dependent on laser wavelength.

The response function, $R(\omega\tau)$ accounts for an attenuated photoacoustic signal when $(\omega\tau) \geq 1$. When $(\omega\tau) << 1$, the relaxation time is short compared to the photoacoustic period and there is no attenuation of signal. However, when the relaxation time approaches an acoustic period, the amount of heat deposited decreases and only a fraction of the energy is converted to an acoustic signal.

$$R(\omega\tau) = \frac{\kappa\tau}{1 + i\omega\tau}$$

The relationship above assumes a two-state system in which the analyte is optically excited from a ground state to an excited state and then undergoes collisional decay back down to the ground state. However, the oxygen A-band is a more complicated three-level system. The molecule is excited from the ground state, $X^3\Sigma_g^-(0,0)$, to the $b^1\Sigma_g^+$ state. It can then undergo collisional relaxation to either the ground state, or the $a^1\Delta_g$ state.

In the case of oxygen, the relaxation time from the b to a state is shorter than an acoustic period, while the relaxation times from b to X and a to X are much longer. Therefore, the system can be approximated as a two-state system with an addition term to account for the energy lost in the process. In this case,

$$R(\omega\tau) = \frac{\kappa\tau\epsilon}{1 + i\omega\tau}$$

where ϵ accounts for the fact that only a portion of the optical energy put into the system can be converted to acoustic energy to produce a photoacoustic signal. In the case of the A-band, $\epsilon \simeq 0.4$. The relaxation function and the observation of the frequency dependence of the function will be discussed further in Section 2.7.

2.4 Experimental Design

The photoacoustic spectrometer is based on a NIST design [11] with several improvements to increase the signal to noise of the data. A schematic of the instrument is displayed in Figure 4.5. An external cavity diode laser (Sacher Lasertechnik ECDL, model TEC520), tunable from 758-770 nm is fiber coupled into a 99:1 PM fiber splitter (Thorlabs, PN780R1A1). The laser frequency is measured with an absolute uncertainty of 2 MHz from the 1% of light directed to a wavemeter (High Finesse, WSU-2) referenced to a frequency stabilized HeNe (Micro-g Lacoste, ML-1) with 100 kHz long-term stability. The remaining 99% of the laser power (~ 20 mW) seeds a tapered amplifier (New Focus, TA-7613) with a free-space output of 800 mW. Two lenses form a Galilean telescope to focus the light on an acousto-optic modulator (Brimrose, TEM 110-25) and the intensity modulated laser beam is collimated and sent through the photoacoustic cell housed in a vacuum chamber.

As described by Gillis[11], the stainless steel photoacoustic cell consists of a 100 mm long, 6 mm diameter resonator between a pair of 50 mm long, 30 mm diameter cylindrical baffle chambers. An electret microphone (PUI Audio, POM-5038L-C3310-R) sits at the center of the resonator. Flanges at each end mount wedged 0.5" windows (Thorlabs WW40530-B) used to limit etalon issues. The window seal is formed with flourosilicone o-rings to allow for future measurements at temperatures down to 200K. The cell is enclosed in a vacuum chamber to limit acoustic noise and ambient temperature fluctuations.

The laser modulation frequency is set to excite the lowest order longitudinal mode of the acoustic resonator (typically 1.5-1.6 KHz) in order to maximize the signal to noise of the acquired spectra. The resonant frequency is sensitive to changes pressure, temperature or gas composition, so before each scan, the optical frequency of the laser is tuned to an absorption peak, and the modulation frequency is scanned over a wide range (500-2500 Hz) to properly set the modulation frequency. The measured Q factors vary slightly with pressure, but are typically ~ 20 at ambient pressure.

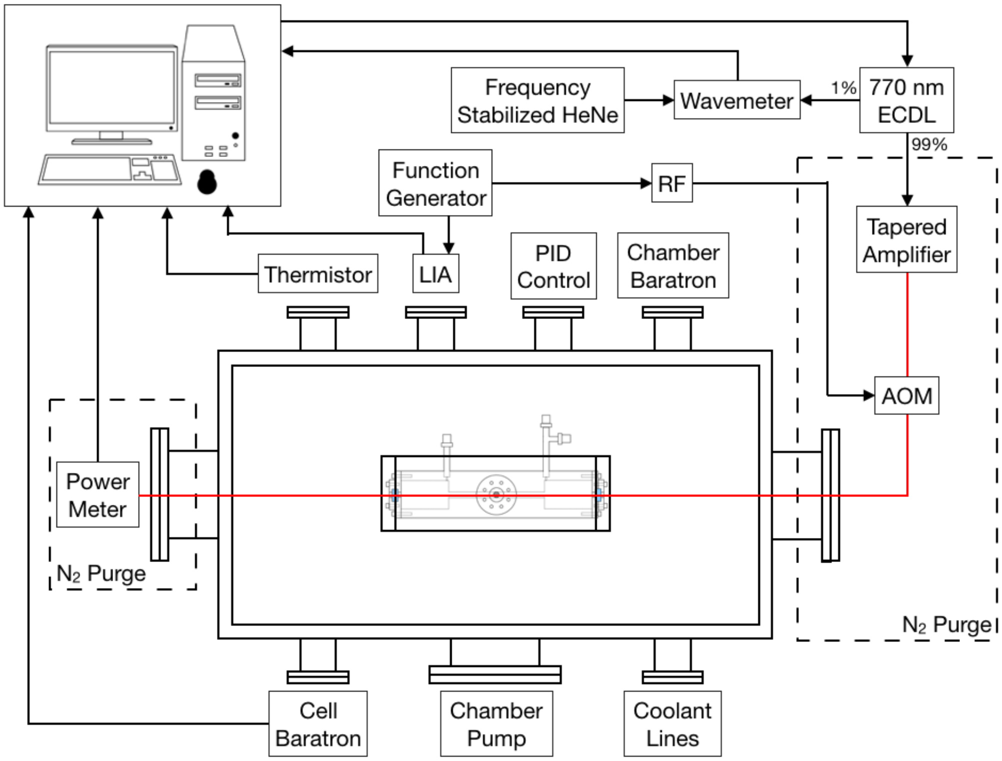

Figure 2.1: Graphic illustration of the PAS experiment

The cell is enclosed in an aluminum housing equipped with 3 custom designed stainless steel/Macor legs mounted to a 12” × 24” optical breadboard to maximize stability and minimize thermal contact with the external environment. This breadboard is placed in a 12” × 12” × 24” custom designed stainless steel vacuum chamber (Kurt J. Lesker Company). The short ends of the chamber are equipped with 6" Conflat flanges which hold 1.5" viewports (Thorlabs VPCH42-B) to allow beam transmission. Each long side has four 2 3/4" Conflat flanges and one 6" Conflat flange. A 1.5" butterfly valve (MDC Vacuum Products 360001) is fixed to one of the 6" Conflat ports to allow for high throughput pump out of the chamber. A 2 3/4" CF flange with two UHV welded 1/4" tubes with VCR connections (Kurt J. Lesker LFT322MVFV) is used for cell gas fill/pumpout lines. A multi-pin bayonet feedthrough is used to carry the four wire Pt RTD signal and a 2 3/4" CF BNC feedthrough is used for the microphone signal.

The beam exiting the vacuum chamber is directed to a silicon photodetector (Newport 918D-SL-OD3) which measures the peak-to-peak power after the cell. This measured power is corrected for absorption along half of the cell pathlength to normalize the photoacoustic signal to the power at the center of the cell where the microphone is mounted. Two polycarbonate boxes are placed over the beam path both before and after the chamber so that the entire free-space beam path can be purged with nitrogen. A-band absorption by the ambient air along the beam path attenuates the power; however, correcting the power requires knowledge of the lineshape being measured. Therefore, the attenuation problem was minimized to a negligible amount by purging the path with nitrogen.

The cell pressure is monitored with a heated capacitance manometer (MKS 690A) with an uncertainty of 0.08% of the reading up to 10,000 Torr. The temperature was measured with a calibrated Pt RTD with 0.1K uncertainty mounted on the cell in direct contact with the gas sample.

The cell and gas lines were heated to $35°C$ and pumped down with a turbo pump for 4 days to reach a base pressure of about 2×10^{-5} Torr. Efforts were made to limit the amount of water because water efficiently quenches the relaxation mechanism giving rise to the photoacoustic signal. Dry samples were used to minimize both complications in accounting for the response and possible perturbations to the lineshape profiles.

2.5 Automated Scanning for Full Band Measurements

The data acquisition is fully automated so that no intervention is required over the course of a single scan ($\sim$ 20 hours). A full band ($\sim$ $190cm^{-1}$) scan consists of $\sim$ $15,000$ data point with 400MHz (0.0133 cm^{-1}) spacing between points. A frequency set point is generated in the custom LabVIEW program, and a PID lock loop based on the wavemeter reading (170 Hz) adjusts parameters to lock the laser frequency to the set point. Fine adjustments are done by tuning the current on the diode while larger corrections are controlled by adjusting the piezo voltage on the cavity of the ECDL. After the standard deviation of the measured wavelength has been <1MHz for 50 consecutive points, the laser is considered locked and data acquisition begins. The pressure and temperature is recorded at every point. In addition the program rapidly alternates between collecting microphone voltages and power meter readings in order to limit the noise introduced by long term power fluctuations. A single point takes approximately 5 seconds, with the stepping and locking of the laser frequency requiring $\sim$ 4 seconds and $\sim$ 1 second averaging time of microphone/power data. In addition, the LabVIEW code corrects for mode hops by adjusting the DC diode current to allow for the broadband, uninterrupted spectra.

2.6 Temperature Control

A temperature control system with the goal of stabilizing the gas sample temperature to $< 0.1\%$ over the course of 21 hours. The cell is enclosed in a custom designed aluminum housing with close thermal contact at all surfaces (drawings in Appendix B). This housing is mounted on 3 Macor rod mounts in order to limit thermal contact with the environment. Each rod is capped with a custom-designed stainless steel 2-piece mount (drawings in Appendix C) in order to isolate the sample from fluctuations in ambient temperature. The cell is then enclosed in a custom stainless steel vacuum chamber (drawings in Appendix A). The housing has four symmetrically placed flow channels to allow for coolant flowing while minimizing gradients. For temperatures slightly below room temperature ($270<T<300$), a 50:50 ethylene glycol/water mix was prechilled to -20^{o}C in a Thermo Neslab RTE-7 chiller/circulator. The prechilled fluid was then flowed through copper coils submerged in a -20^{o}C (Thermo Scientific CB-80). The coolant then flows through a liquid nitrogen feedthrough on the chamber, is split to flow symmetrically throught the housing and exits the chamber to return to the RTE-7. The aluminum housing has three pieces of Kapton flexible heating tape self-adhered to the surfaces (Omega, KH-303/5-P, KH-306/5-P). The tape is connected to a PID controller using a surface mount thermistor mounted to the cell housing to determine the error signal compared to a desired set point. The resulting cool down time and stability for this set-up is shown in Figure 2.2. It takes approximately 24 hours for the gas sample temperature to stabilize, but once stabliized, the temperature remains constant to ±25mK over a typical scan time of 21 hours.

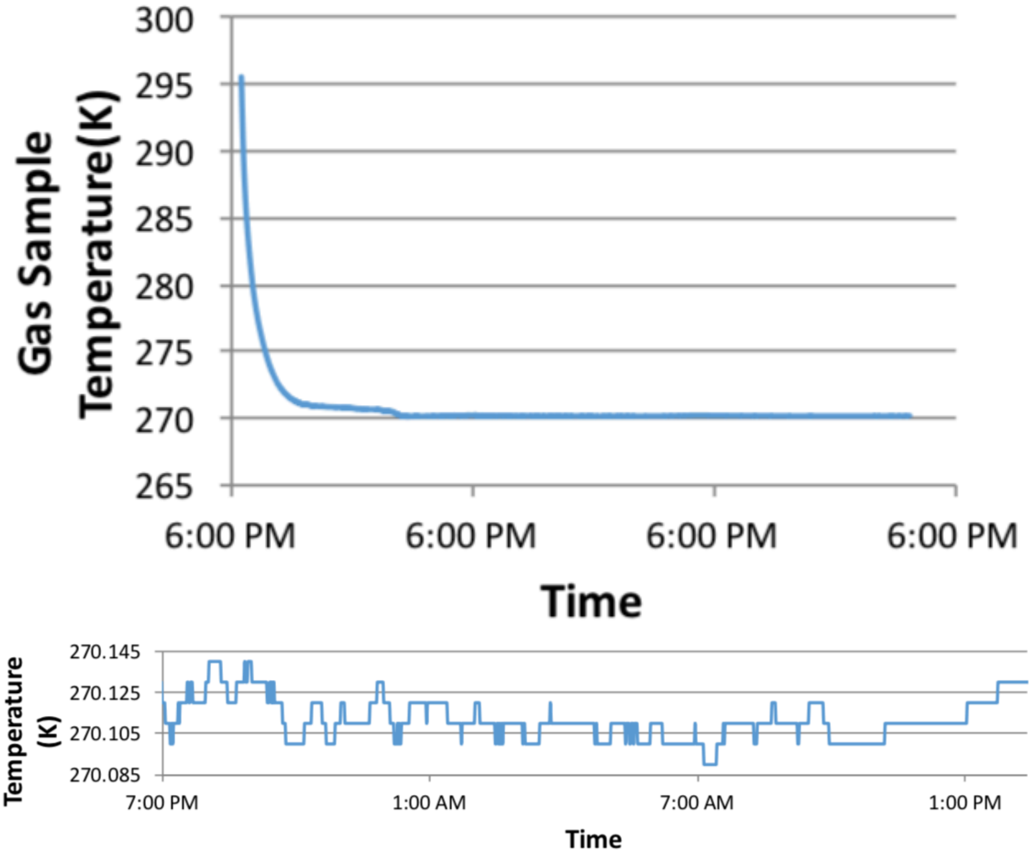

Figure 2.2: Measured temperature of gas sample showing a cool down time of about 24 hours (top) and the measured gas sample temperature over the course of a scan demonstrating a stability of $\pm 25 mK$

2.7 Characterizing Instrument Response

One of the most challenging aspects of retrieving quantitative information from the photoacoustic data was converting the microphone signal to absolute absorption. Figure 2.3a shows a measured PAS spectrum for 500 Torr of oxygen. The fitted intensities relative to Drouin 2017 are displayed in Figure 2.3b. While the SNR of the spectrum is over 20,000, the relative intensities show a clear deviation from previously measured values on the order of 2%. Some of this change in response across the spectrum can be explained by the proportion of optical energy that is possible to be released as acoustic energy due to the approximation of the 3-state system as a 2-state system. As discussed in Section 2.3, ϵ in the following equation is approximately 0.4.

$$R(\omega\tau) = \frac{\kappa\tau\epsilon}{1 + i\omega\tau}$$

ϵ is defined as the percentage of optical energy which can be released as acoustic energy. It is often approximated as:

$$\epsilon = \frac{\nu_{ba}}{\nu_{bX}}$$

However, as the laser tunes across the spectrum, the amount of optical energy is changing and should not be approximated as ν_{bX}. When ϵ is instead defined as:

$$\epsilon = \frac{\nu_{las} - \nu_{aX}}{\nu_{las}}$$

where ν_{las} is the laser frequency, the expected response function is shown in Figure 2.3c. This definition of ϵ assumes rapid thermalization of rotational states in the b state, a relaxation to v=0 of the a-state and finally rapid thermalization of rotational states within the a state. This is reasonable under the experimental conditions. It is linear across the spectrum and only depends on the frequency of the laser. Figure 2.3d shows the resulting relative intensities after the data is corrected for the frequency-dependent response described above. Notably, something resembling a J-dependent response remains. It is likely that this remaining response is due to a J-dependent collisional relaxation rate constant impacting the overall signal through $R(\omega\tau)$:

$$R(\omega\tau) = \frac{\kappa\tau}{1 + i\omega\tau}$$

Unfortunately, the response function could not be characterized within the signal to noise of the data and would be the limiting factor in data analysis if the approach of fully correcting the data according to a functional form was attempted. Therefore, after the data was corrected for the known frequency-dependent response, the intensities of indiviual lines were allowed to float in all fitting procedures in order to account for the J-dependent response function.

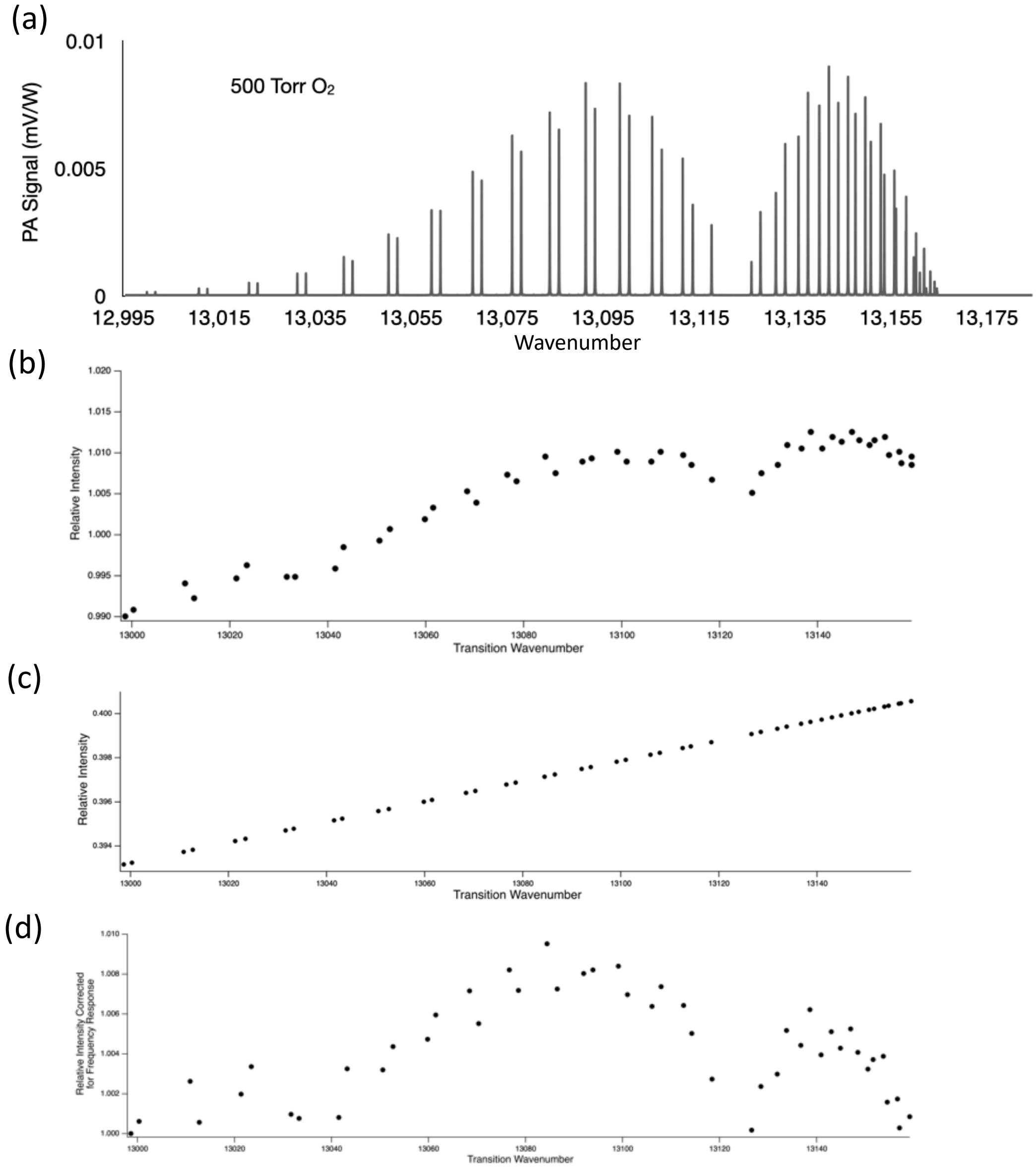

Figure 2.3: Measured A-band spectrum of 500 Torr oxygen (a), the ratio of the fitted intensity relative to Drouin 2017 as a function of transition wavenumber (b), the expected frequency dependent response based on the photoacoustic signal generation model presented (c) and the remaining relative intensities after data is corrected for the frequency dependent response which is attributed to a J-dependent collisional relaxation rate constant

2.8 Instrument Performance

The Allan deviation for the instrument is shown in Figure 2.3. Excellent long-term stability is demonstrated with no evidence of long-term drift at 3,000 samples or about 11 minutes of averaging time. We calculate an α_{min} of $1.3 \times 10^{-9} cm^{-1}$ and a NEA of $2.1 \times 10^{-8}\mathrm{cm}^{-1}\mathrm{Hz}^{-1/2}$. However, there is a need to balance sensitivity with data acquisition time. If we were to attempt to achieve maximum sensitivity, a single scan would take 52 days. This is clearly impractical and also introduces additional experimental challenges in terms of accounting for long-term drift in pressure, temperature or other conditions. Therefore, we chose to acquire 15 samples per data point. This results in an α_{min} of $1.2 \times 10^{-8} cm^{-1}$ and allows for a single spectrum to be collected in approximately 20 hours.

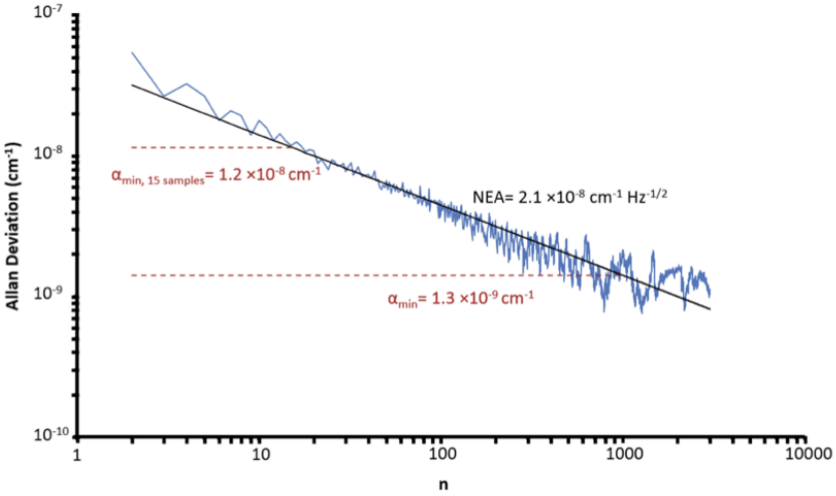

Figure 2.4: O_2 PAS Allan deviation

Figure 2.3 demonstrates the dynamic range of the instrument due to the long-term stability and long-term averaging possible. The full scale of the spectrum on the right is four orders of magnitude weaker than the spectrum on the left and still has signal to noise of about 50.

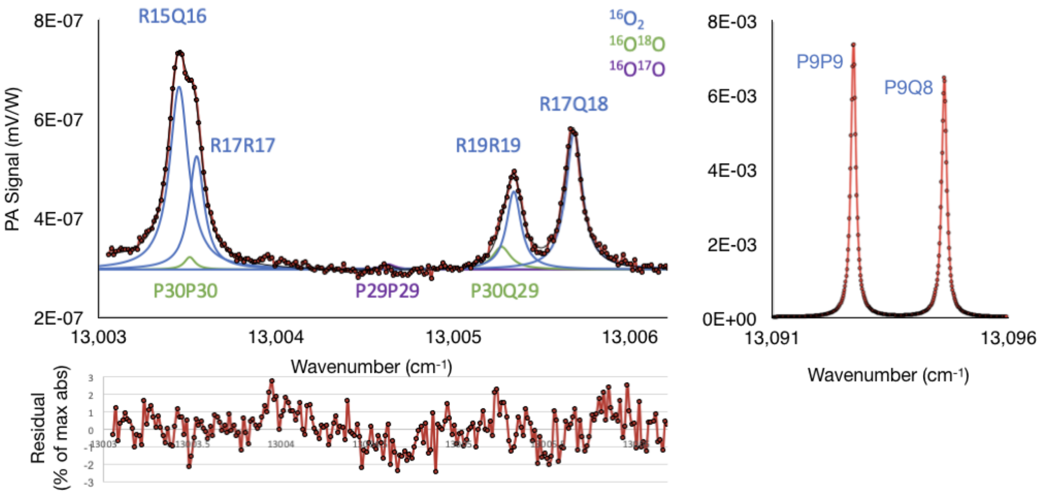

Figure 2.5: Demonstration of dynamic range of PAS

Figure 2.4 shows the 500 Torr pure oxygen spectrum and residual in comparison to FTS data to demonstrate the improvement in signal to noise and ability to observe subtle lineshape effects which may not be evident in FTS data.

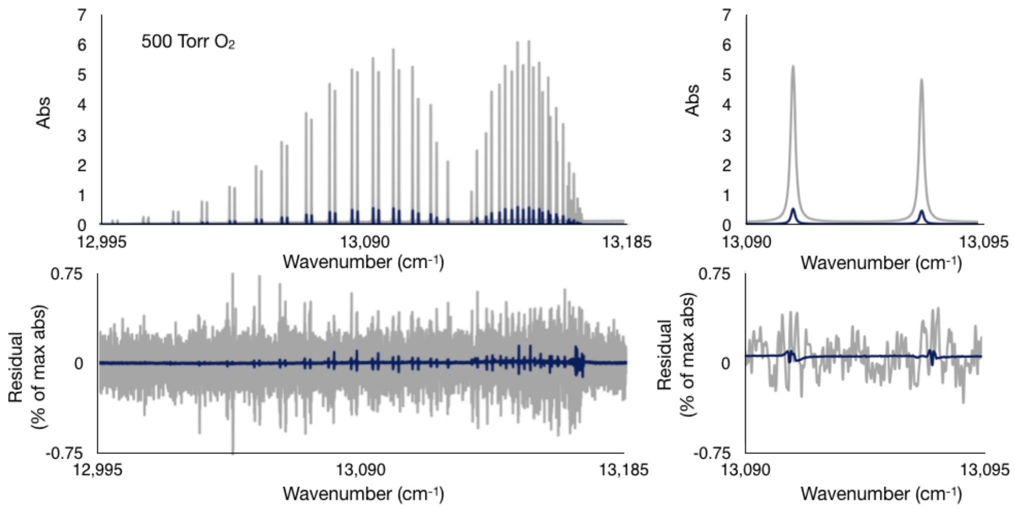

Figure 2.6: SNR comparison to FTIR

Figures 2.5 and 2.6 show the measured spectra over a range of pressures for both pure oxygen and NIST air. Oxygen was measured from 50-3000 Torr and air was measured from 100-4000 Torr. Signal-to-noise is pressure and composition dependent and ranges from 7,000-50,000.

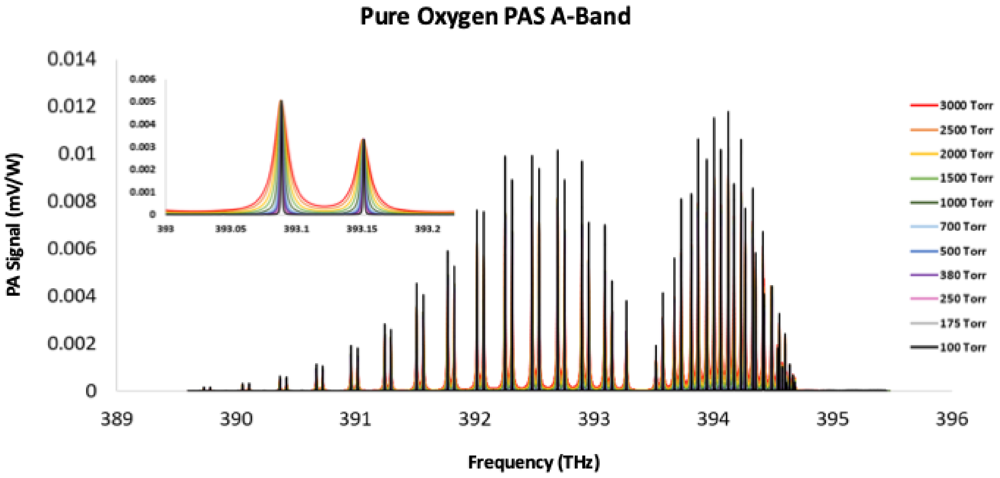

Figure 2.7: All room temperature pure oxygen spectra

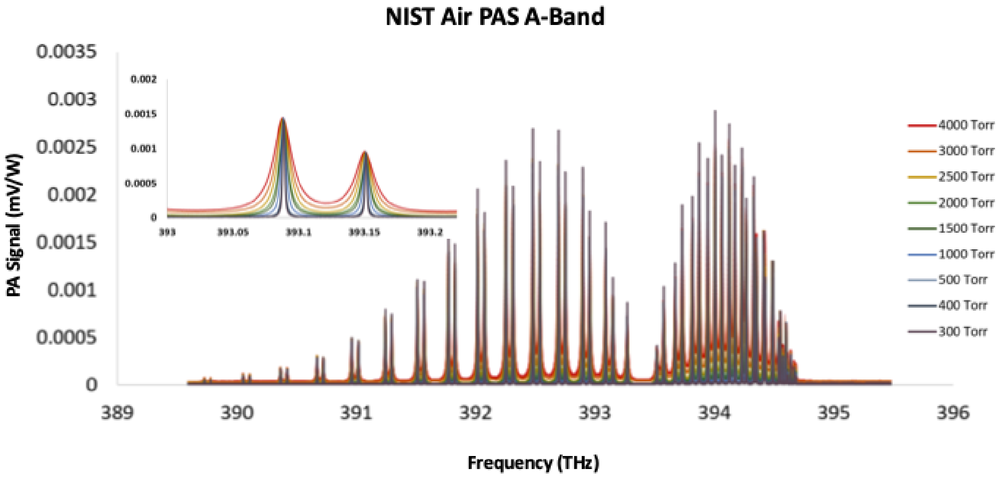

Figure 2.8: All room temperature air spectra

BIBLIOGRAPHY

[1] H. Tran, C. Boulet, and J.-M. Hartmann. “Line mixing and collision-induced absorption by oxygen in the A band: Laboratory measurements, model, and tools for atmospheric spectra computations”. In: *Journal of Geophysical Research: Atmospheres* 111 (D15 2006). ISSN: 2156-2202. DOI: 10.1029/2005JD006869.

[2] H. Tran and J.-M. Hartmann. “An improved O2 A band absorption model and its consequences for retrievals of photon paths and surface pressures”. In: *Journal of Geophysical Research: Atmospheres* 113 (D18 2008). ISSN: 2156-2202. DOI: 10.1029/2008JD010011.

[3] Frans R. Spiering et al. “Collision-induced absorption in the O2 B-band region near 670 nm”. In: *Physical Chemistry Chemical Physics* 13.20 (May 3, 2011), pp. 9616–9621. ISSN: 1463-9084. DOI: 10.1039/C1CP20403C.

[4] Frans R. Spiering and Wim J. van der Zande. “Collision induced absorption in the a1(v = 2) X3g(-)(v = 0) band of molecular oxygen”. In: *Physical chemistry chemical physics: PCCP* 14.28 (July 28, 2012), pp. 9923–9928. ISSN: 1463-9084. DOI: 10.1039/c2cp40961e.

[5] Frans R. Spiering et al. “Line mixing and collision induced absorption in the oxygen A-band using cavity ring-down spectroscopy”. In: *The Journal of Chemical Physics* 133.11 (Sept. 21, 2010), p. 114305. ISSN: 0021-9606. DOI: 10.1063/1.3460924.

[6] D. A. Long, D. J. Robichaud, and J. T. Hodges. “Frequency-stabilized cavity ring-down spectroscopy measurements of line mixing and collision-induced absorption in the O2 A-band”. In: *The Journal of Chemical Physics* 137.1 (July 5, 2012), p. 014307. ISSN: 0021-9606. DOI: 10.1063/1.4731290.

[7] Brian J. Drouin et al. “Multispectrum analysis of the oxygen A-band”. In: *Journal of quantitative spectroscopy & radiative transfer* 186 (Jan. 2017), pp. 118–138. ISSN: 0022-4073. DOI: 10.1016/j.jqsrt.2016.03.037.

[8] Tijs Karman, Ad van der Avoird, and Gerrit C. Groenenboom. “Line-shape theory of the X3ga1g,b1g+ transitions in O2–O2 collision-induced absorption”. In: *The Journal of Chemical Physics* 147.8 (Aug. 28, 2017), p. 084307. ISSN: 0021-9606. DOI: 10.1063/1.4990662.

[9] Tijs Karman et al. “O2O2 and O2N2 collision-induced absorption mechanisms unravelled”. In: *Nature Chemistry* 10.5 (May 2018), pp. 549–554. ISSN: 1755-4330, 1755-4349. DOI: 10.1038/s41557-018-0015-x.

[10] Tijs Karman, Ad van der Avoird, and Gerrit C. Groenenboom. “Potential energy and dipole moment surfaces of the triplet states of the O2(X3g) O2(X3g,a1g,b1g+) complex”. In: *The Journal of Chemical Physics* 147.8 (Aug. 28, 2017), p. 084306. ISSN: 0021-9606. DOI: `10.1063/1.4990661`.

[11] Tijs Karman et al. “O2O2 and O2N2 collision-induced absorption mechanisms unravelled”. In: *Nature Chemistry* 10.5 (May 2018), pp. 549–554. ISSN: 1755-4330, 1755-4349. DOI: `10.1038/s41557-018-0015-x`.

[12] K. A. Gillis, D. K. Havey, and J. T. Hodges. “Standard photoacoustic spectrometer: Model and validation using O2 A-band spectra”. In: *Review of Scientific Instruments* 81.6 (June 1, 2010), p. 064902. ISSN: 0034-6748. DOI: `10.1063/1.3436660`.

[13] D. Chris Benner et al. “A multispectrum nonlinear least squares fitting technique”. In: *Journal of Quantitative Spectroscopy and Radiative Transfer* 53.6 (June 1, 1995), pp. 705–721. ISSN: 0022-4073. DOI: `10.1016/0022-4073(95)00015-D`.

Appendix A

CHAMBER CAD DRAWINGS

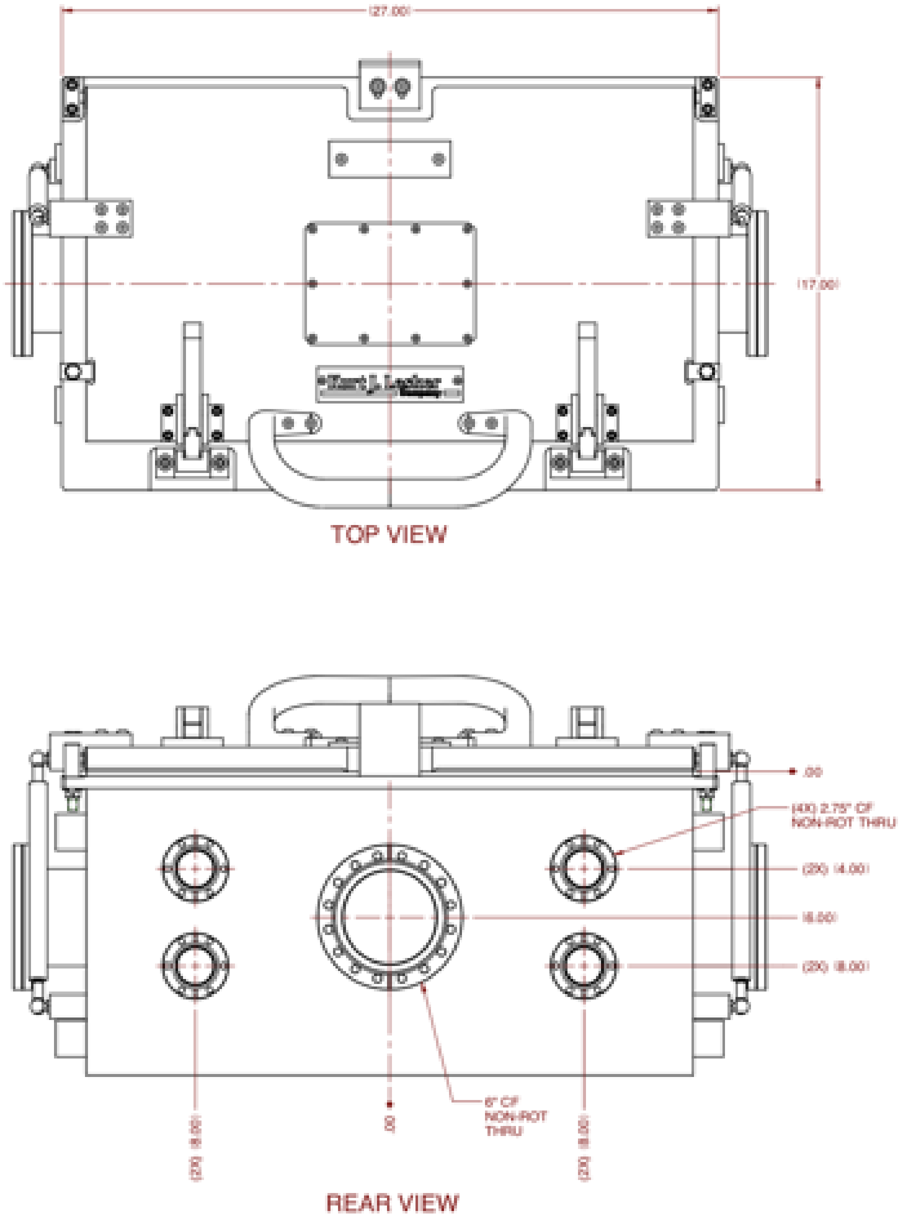

Figure A.1:

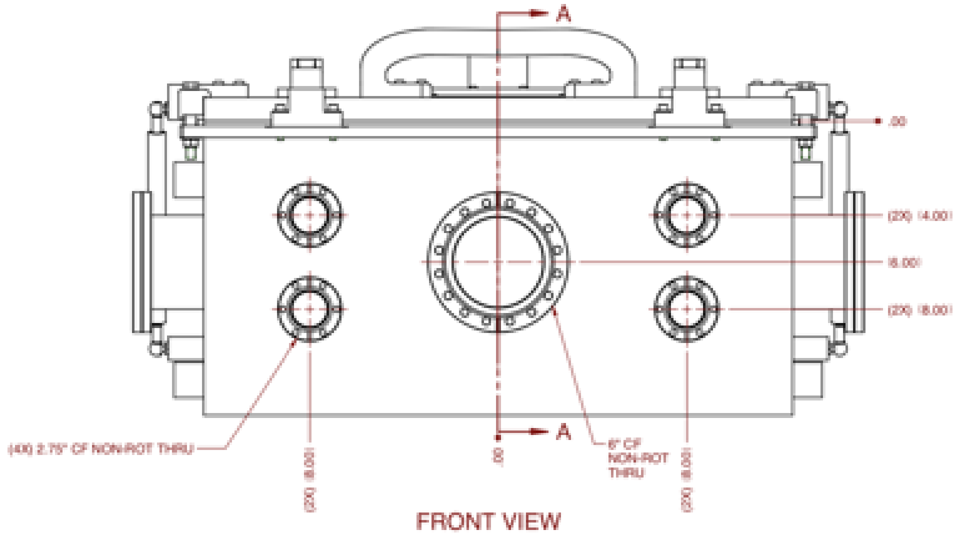

FRONT VIEW

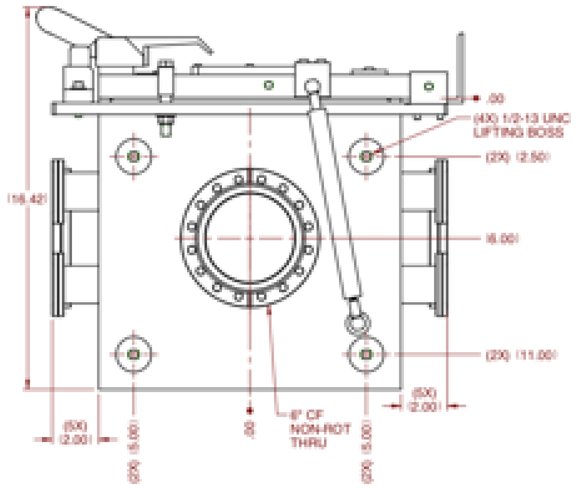

RIGHT SIDE VIEW

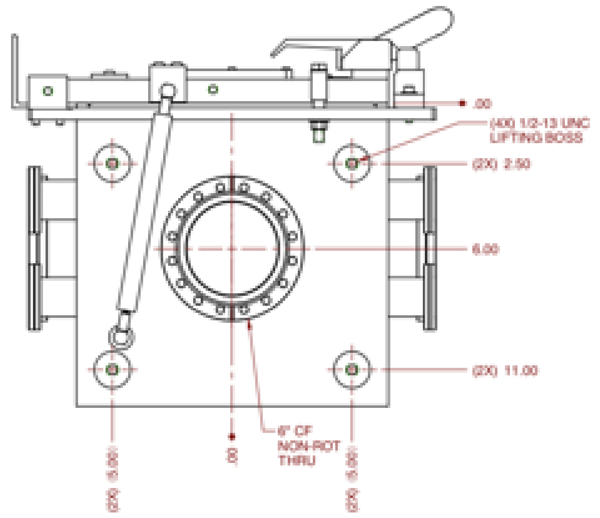

LEFT SIDE VIEW

Figure A.2:

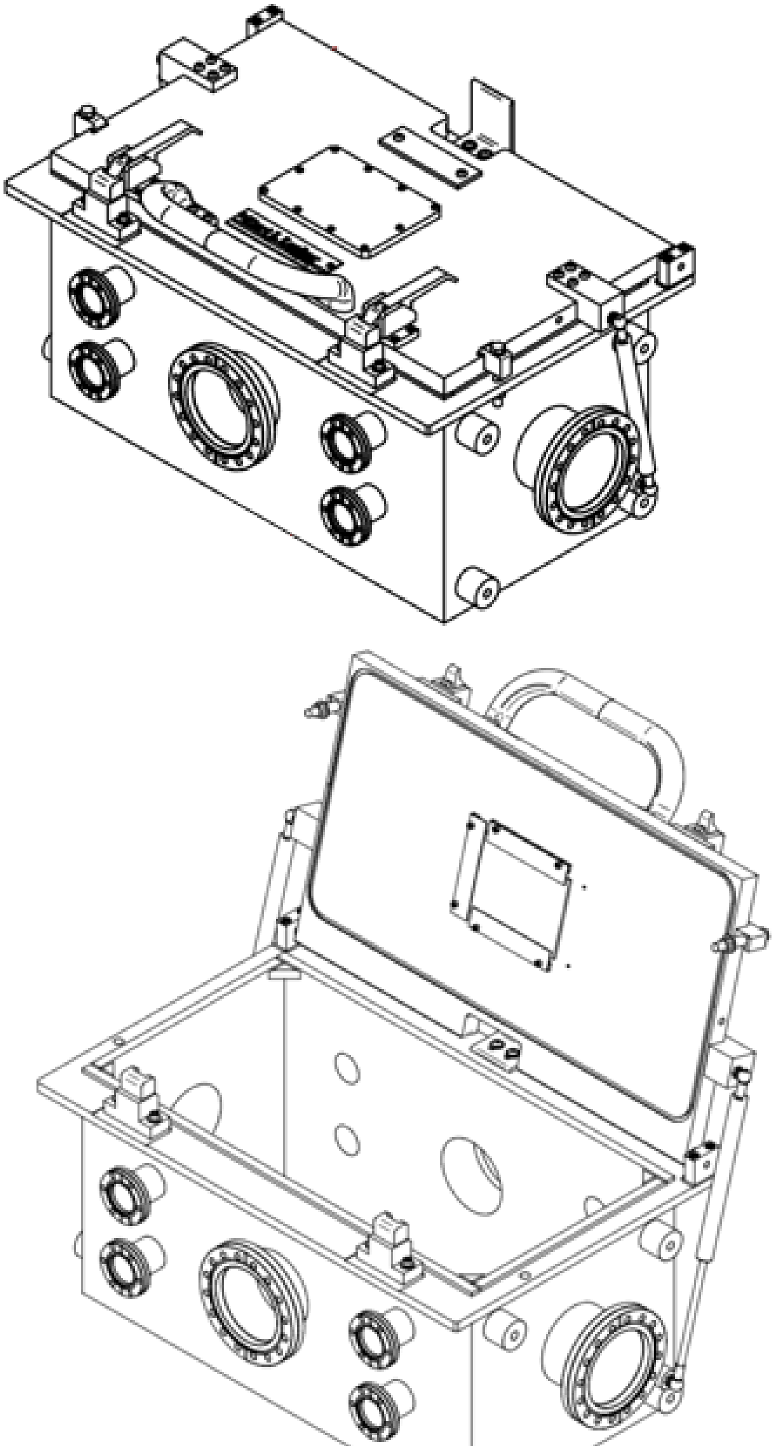

Figure A.3:

Appendix B

HOUSING CAD DRAWINGS

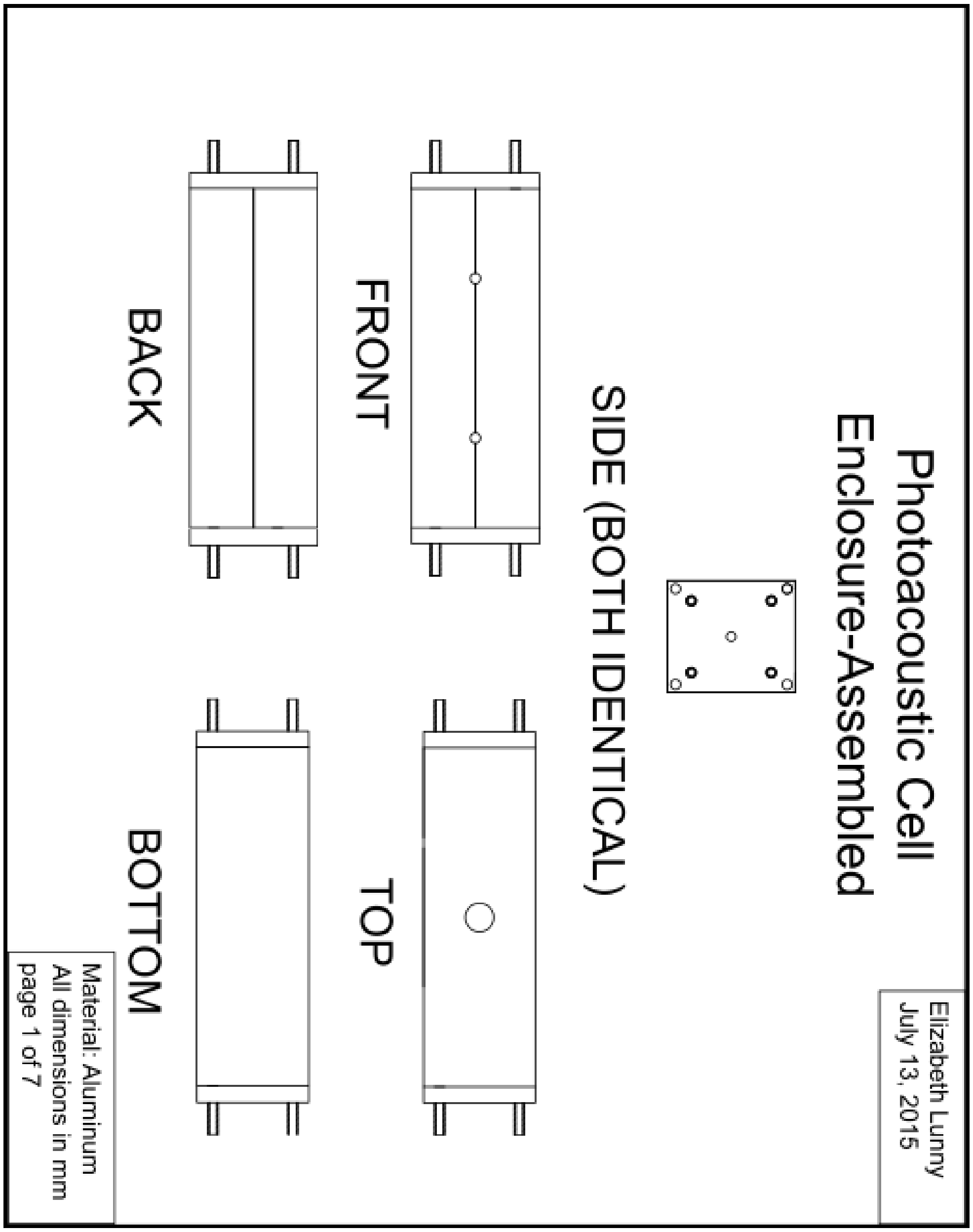

Figure B.1:

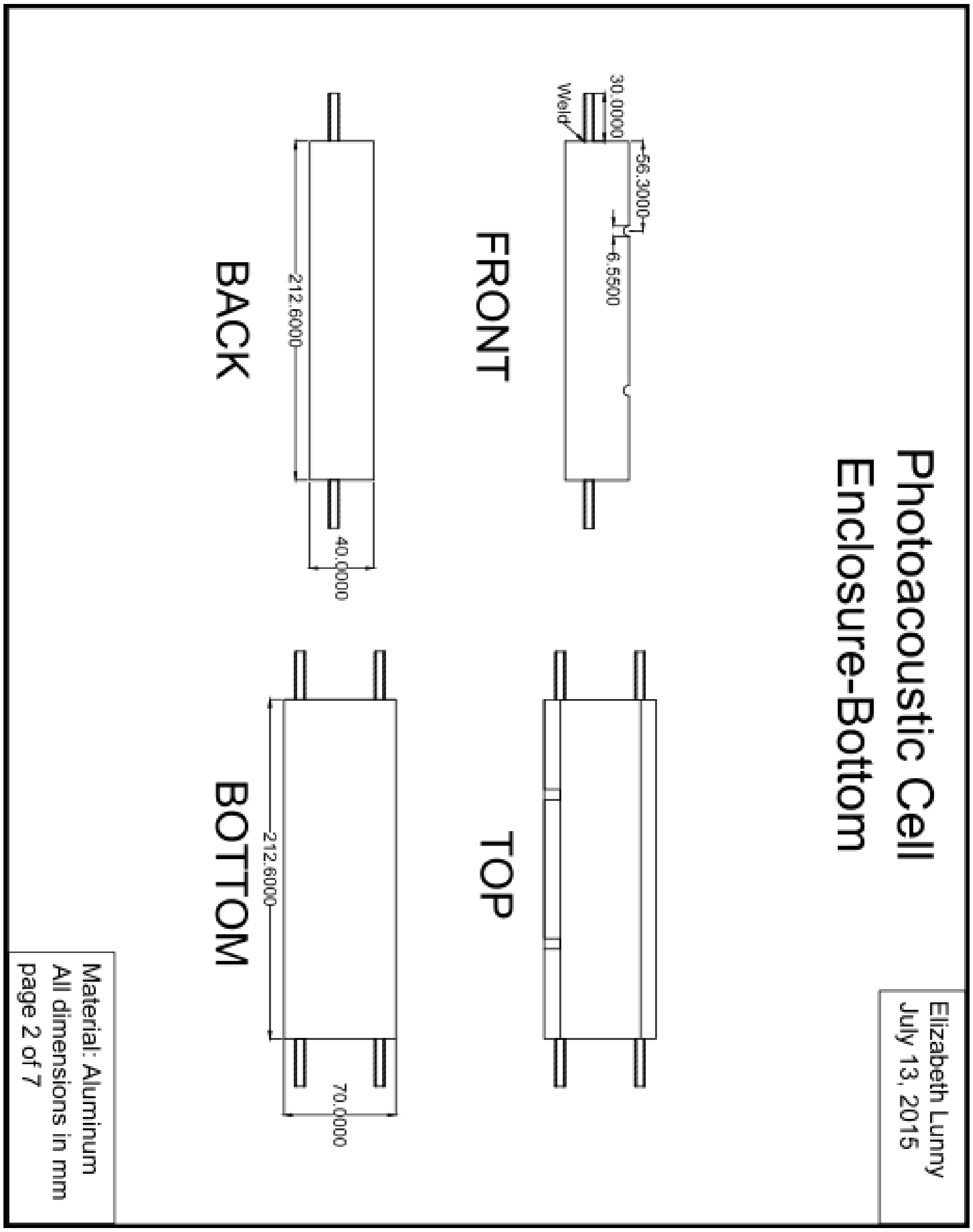
Photoacoustic Cell
Enclosure-Bottom
Elizabeth Lunny
July 13, 2015
FRONT
30.0000
Weld
56.3000
6.5500
BACK
212.6000
40.0000
TOP
BOTTOM
212.6000
70.0000
Material: Aluminum
All dimensions in mm
page 2 of 7

Figure B.2:

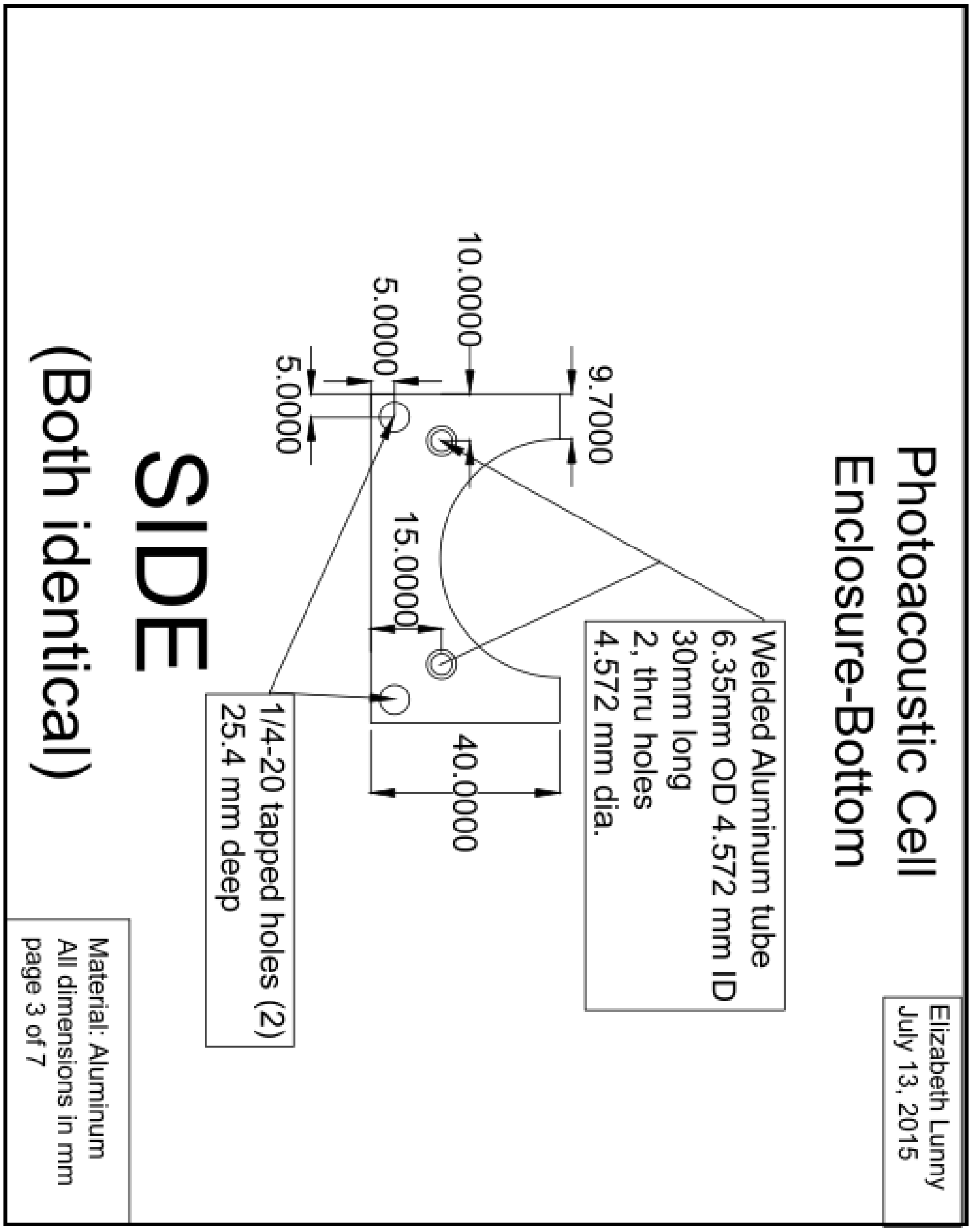
Photoacoustic Cell
Enclosure-Bottom
Elizabeth Lunny
July 13, 2015
Welded Aluminum tube
6.35mm OD 4.572 mm ID
30mm long
2, thru holes
4.572 mm dia.
9.7000
10.0000
5.0000
5.0000
5.0000
15.0000
40.0000
1/4-20 tapped holes (2)
25.4 mm deep
SIDE
(Both identical)
Material: Aluminum
All dimensions in mm
page 3 of 7

Figure B.3:

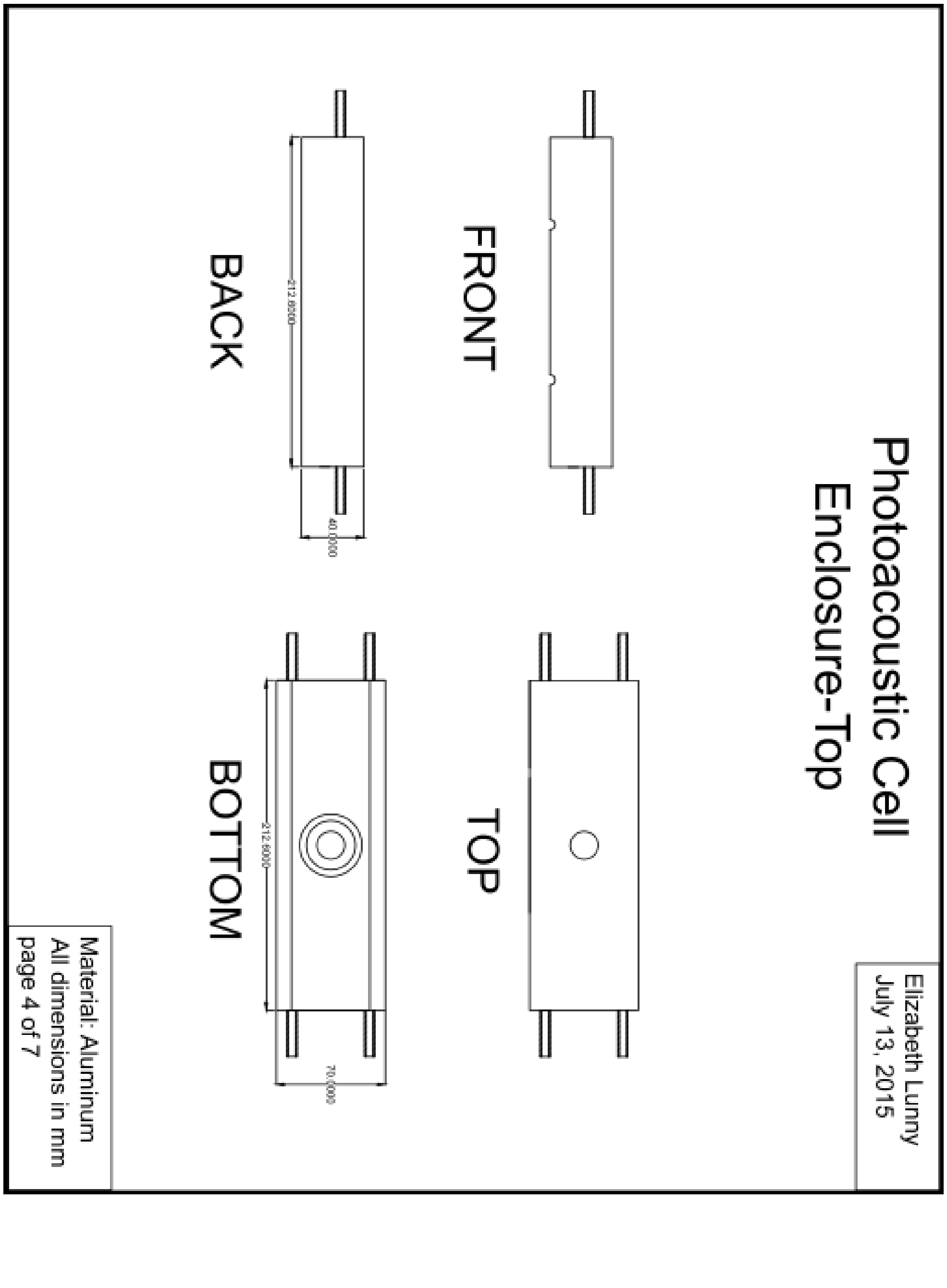
Photoacoustic Cell
Enclosure-Top
FRONT
BACK
TOP
BOTTOM
212.6500
40.0000
212.6000
70.0000
Elizabeth Lunny
July 13, 2015
Material: Aluminum
All dimensions in mm
page 4 of 7

Figure B.4:

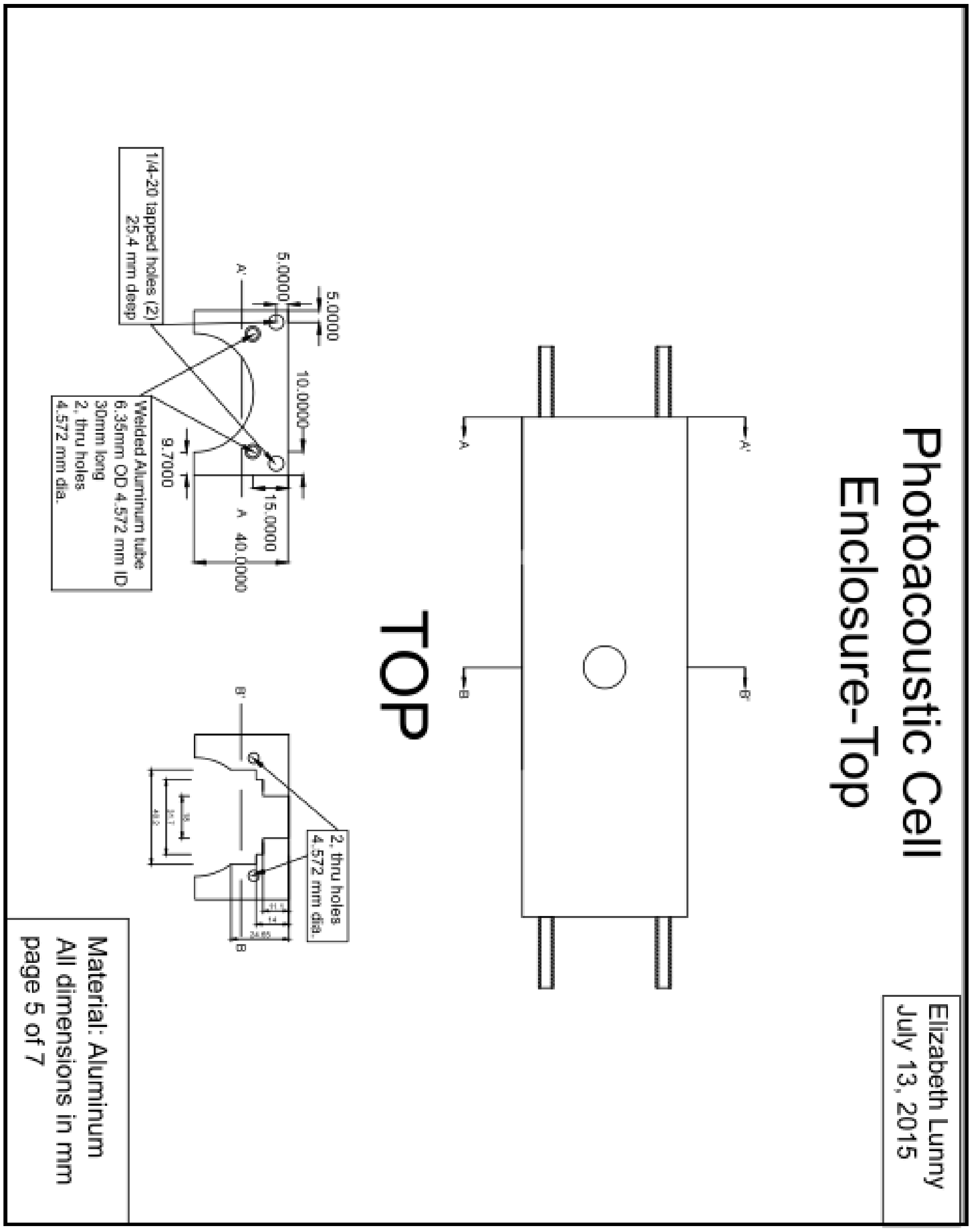
Photoacoustic Cell
Enclosure-Top
Elizabeth Lunny
July 13, 2015
TOP
A
A'
B
B'
1/4-20 tapped holes (2)
25.4 mm deep
5.0000
5.0000
10.0000
9.7000
15.0000
40.0000
Welded Aluminum tube
6.35mm OD 4.572 mm ID
30mm long
2, thru holes
4.572 mm dia.
2, thru holes
4.572 mm dia.
Material: Aluminum
All dimensions in mm
page 5 of 7

Figure B.5:

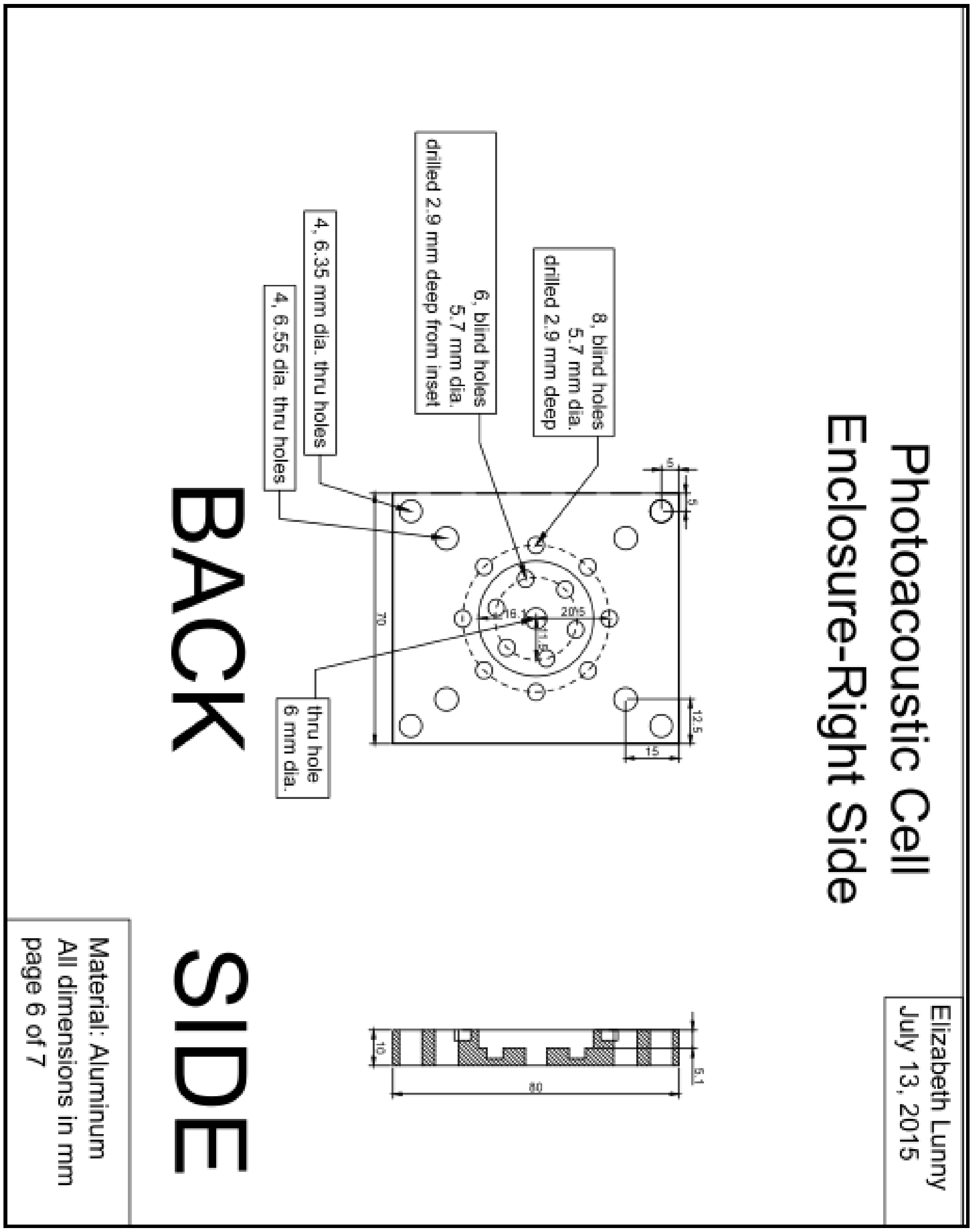
Photoacoustic Cell
Enclosure-Right Side
Elizabeth Lunny
July 13, 2015
8, blind holes
5.7 mm dia.
drilled 2.9 mm deep
6, blind holes
5.7 mm dia.
drilled 2.9 mm deep from inset
4, 6.35 mm dia. thru holes
4, 6.55 dia. thru holes
thru hole
6 mm dia.
5
5
12.5
15
70
16.1
20.5
11.5
10
80
5.1
BACK SIDE
Material: Aluminum
All dimensions in mm
page 6 of 7

Figure B.6:

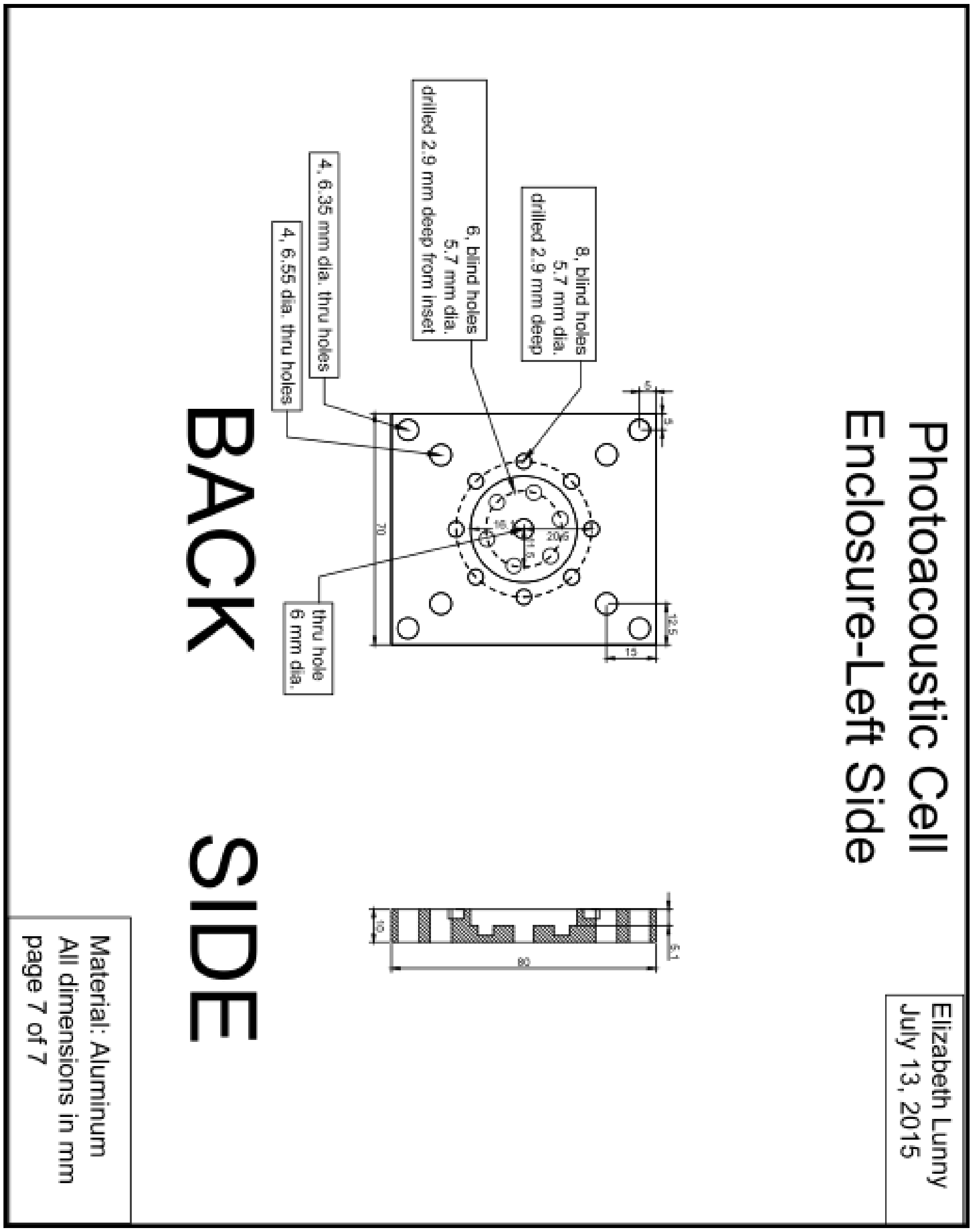
Photoacoustic Cell
Enclosure-Left Side
Elizabeth Lunny
July 13, 2015
8, blind holes
5.7 mm dia.
drilled 2.9 mm deep
6, blind holes
5.7 mm dia.
drilled 2.9 mm deep from inset
4, 6.35 mm dia. thru holes
4, 6.55 dia. thru holes
thru hole
6 mm dia.
5
5
20
12.5
15
10
5.1
80
BACK
SIDE
Material: Aluminum
All dimensions in mm
page 7 of 7

Figure B.7:

Appendix C

HOUSING MOUNT CAD DRAWINGS

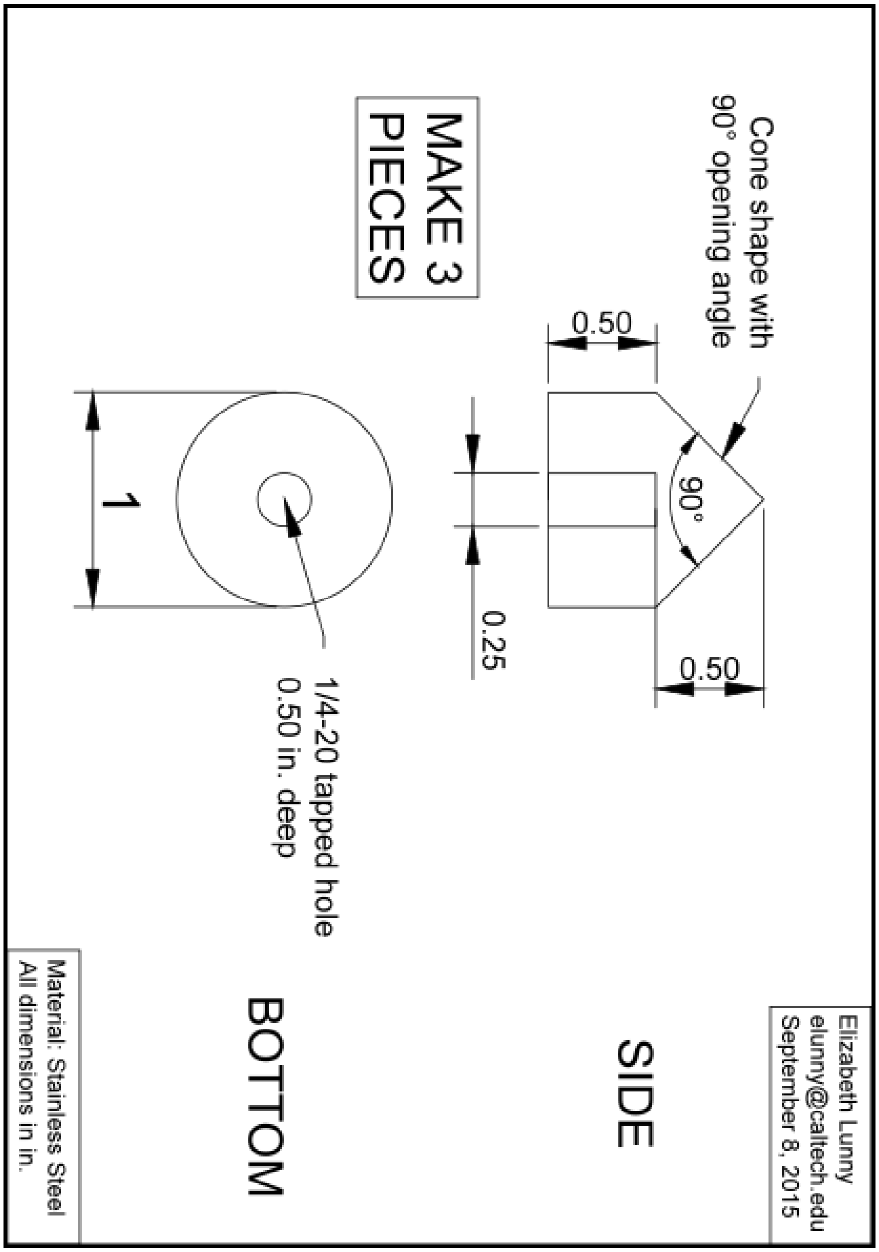

Figure C.1:

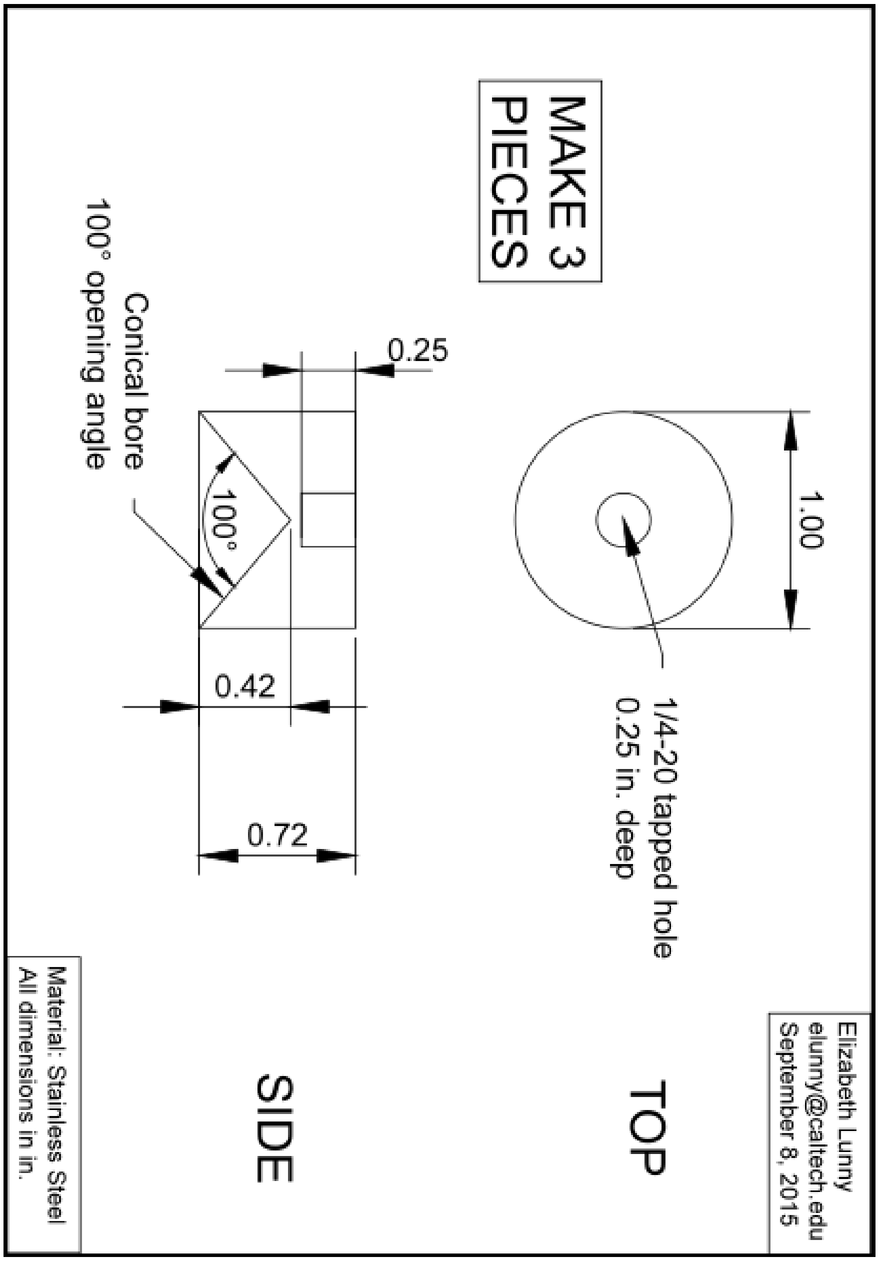
MAKE 3 PIECES
0.25
1.00
100°
Conical bore
100° opening angle
0.42
0.72
1/4-20 tapped hole
0.25 in. deep
TOP
SIDE
Elizabeth Lunny
elunny@caltech.edu
September 8, 2015
Material: Stainless Steel
All dimensions in in.

Figure C.2:

Appendix D

MANIFOLD DESIGN

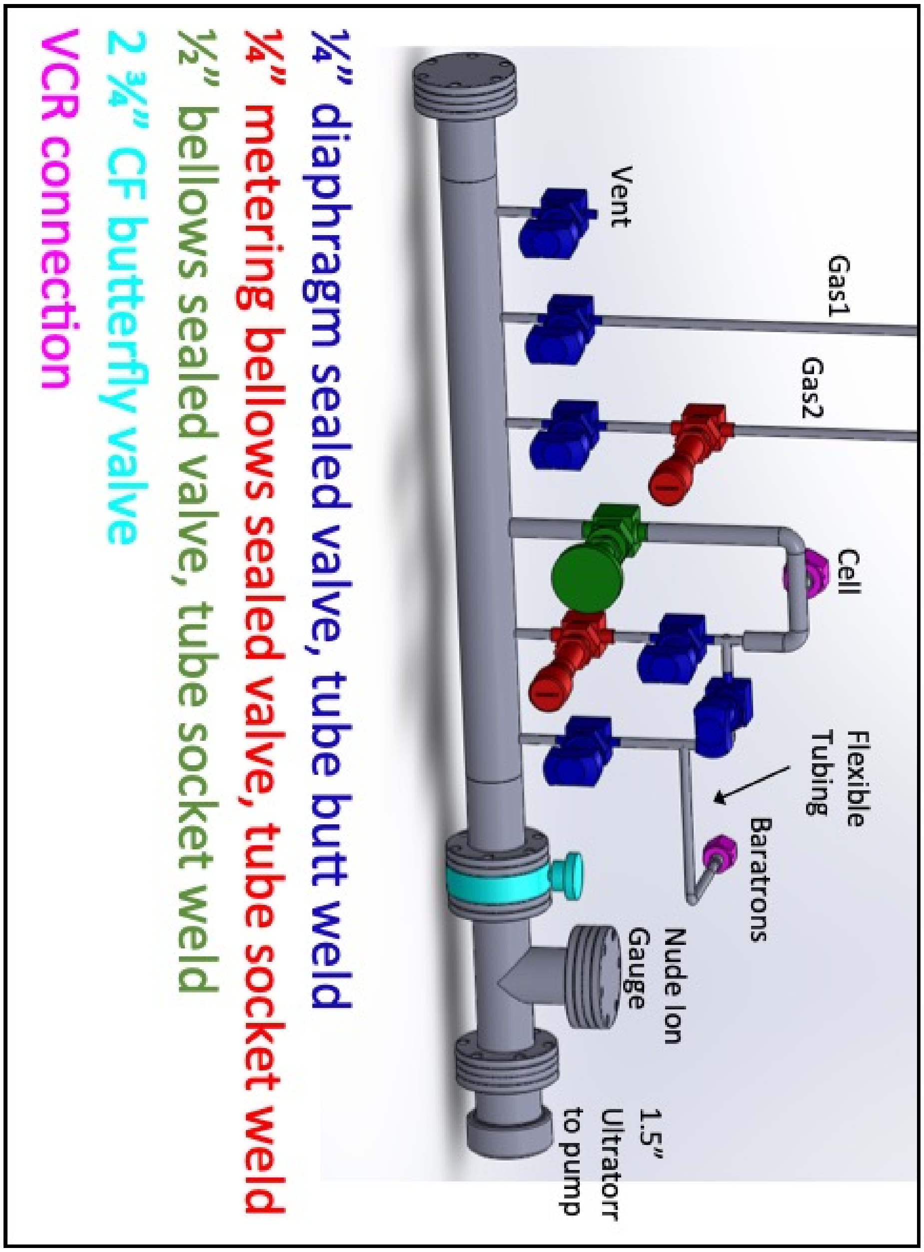

Figure D.1:

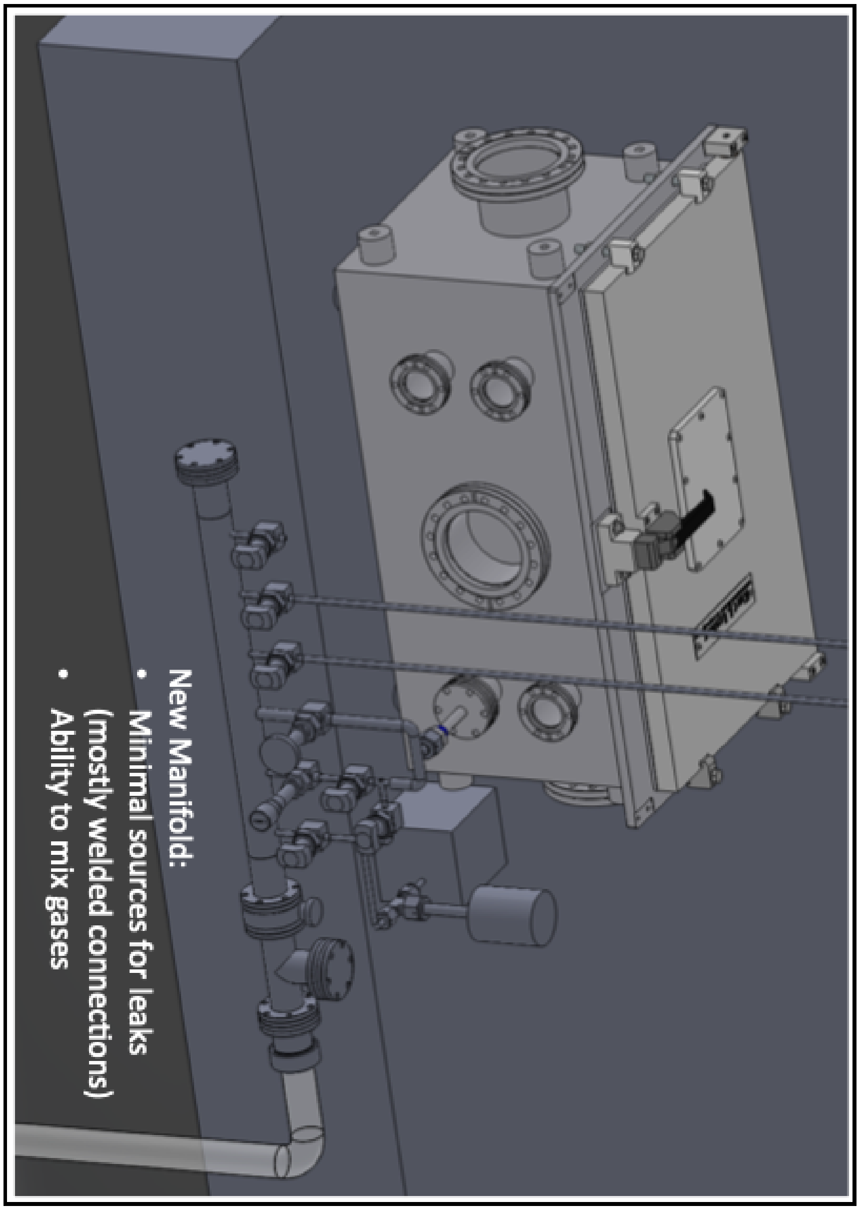

New Manifold:
- Minimal sources for leaks (mostly welded connections)
- Ability to mix gases

Figure D.2:

Appendix E

OPTIMIZING DATA ACQUISITION

One of the critical changes to the data acquisition approach which allowed for the reliable, highly reproducible high signal-to-noise data was in the adjusting the approach to signal averaging. In previous measurements, the photoacoustic signal was measured by acquiring 200 microphone voltage readings from the lock-in amplifier, followed by 20 samples read from the power meter. The photoacoustic signal was then calculated by dividing the average microphone voltage by the average power reading.

$$S = \frac{\frac{\sum_{i=1}^{200} V_i}{200}}{\frac{\sum_{j=1}^{20} P_j}{20}}$$

Microphone voltages are acquired at ~ 500 Hz while the power meter readings are ~ 50 Hz. Therefore, the total data acquisition time for a single data point is about 800 ms with 50% of the time devoted to each type of measurement. While this generally worked well, occasional nonreproducible "spikes" were observed in the residuals when spectra were fit. These "bad points" were rare, occurring approximately 5-8 times in a spectrum of 15,000 data points, but they always occurred on absorption lines, making accurate fits impossible. It was observed that these "bad points" were accompanied by an above average standard deviation in the power measurements.

Further investigations revealed that these spikes arise from short term drift in the laser power. When the power rapidly changes on short timescales, the power can differ by up to a few percent on the hundreds of milliseconds timescale during a measurement. Therefore, the power that is used to normalize the photoacoustic signal is not the same as the actual power that produced that signal resulting in these "bad points".

The averaging approach was adjusted in an attempt to better capture any short term power fluctuations and improve the signal-to-noise ratios of the data.

$$S = \sum_{i=m}^{n} \frac{\frac{\frac{\sum_{i=1}^{50} V_i}{50}}{\frac{\sum_{j=1}^{5} P_j}{5}}}{n}$$

The number of measurement loops acquired (n) is the x-axis in Figure 2.8. In order to achieve a reasonable overall measurement time for the full scan, typically for the measurements shown here, n=15. However, the excellend long-term stability of measurements allows for noise to be averaged down for increasing n over very long time scales (10 minutes) so n can be set accordingly to balance scan time and desired signal to noise ratios.

Chapter 3

DETERMINATION OF PRESSURE SHIFTS OF THE OXYGEN A-BAND USING PHOTOACOUSTIC SPECTROSCOPY

3.1 Abstract

Pressure shift coefficients for P-branch and R-branch transitions of <30 are reported using photoacoustic spectroscopy. The high-resolution spectrometer with an absolute frequency axis uncertainty of 2 MHz provides high SNR data ($\sim 30,000 : 1$) allowing for pressure shift coefficients with the lowest uncertainties reported for the oxygen A-band. Parameters were retrieved for both oxygen and nitrogen by fitting spectra with a pressure range of 50-400 Torr with the Nelkin-Ghatak lineshape profile. These values are critical to accurately predict asymmetric lineshapes needed for remote sensing applications. For example, the OCO missions state an uncertainty goal of $< 0.0002\mathrm{cm}^{-1}/\mathrm{atm}$ which is achieved for the strongest transitions in this study.

3.2 Introduction

Accurate characterization of lineshape parameters for atmospheric species is critical for spectroscopic remote sensing missions. The oxygen A-band (762 nm) is utilized for determination of air mass, solar pathlength and surface pressure in a number of remote sensing applications due to the uniform concentration of molecular oxygen throughout the atmosphere and the spectral isolation of the band. Advancements in remote sensing technologies are placing ever more stringent requirements on the quantification of lineshape parameters. For example, NASA's OCO-2 satellite seeks to retrieve atmospheric column dry mole fractions of carbon dioxide with an accuracy of 1 ppm or about 0.25%. Error in oxygen spectroscopy propagates to retrieved CO_2 mole fractions requiring accurate quantification of the A-band spectral parameters.

In recent years, a number of experimental efforts have greatly improved the accuracy of oxygen A-band lineshape parameters to meet the needs of the OCO missions. Cavity ring-down spectroscopy (CRDS) and Fourier transform spectroscopy (FTS) have been used to determine highly accurate positions [1, 2, 3, 4, 5], intensities [1, 2, 6, 7, 4, 5], nitrogen and self pressure broadened widths [1, 8, 2, 6, 7, 4, 5], nitrogen and self pressure-induced shifts [1, 8, 6, 9, 4, 5], and narrowing parameters[2, 6, 7]. The temperature dependence of these lineshape parameters have also been measured [4, 5]. The sensitivity of many of these measurements requires accurate characterization of isotopologue lineshapes as well [10]. In addition to the efforts to accurately model the isolated lineshape profiles, studies to quantify the high pressure effects of line mixing (LM) and collision-induced absorption (CIA) [11, 12, 5, 13] have also been critical in the development of a spectroscopic model to fit the satellite spectra with the accuracy required to meet mission goals.

Pressure-induced shifts in the oxygen A-band are typically about an order of magnitude smaller than spectral linewidths making accurate measurements difficult. The pressure shift coefficient, $\delta = d\nu/dp$, depends on temperature, collisional partner and J, the total angular momentum. High signal-to-noise data and appropriate lineshape models are necessary for accurate pressure shift measurements. In addition, as Predoi-Cross demonstrated [1], error in the absolute frequency axis can significantly impact the retrieved values. Pressure shift uncertainties $< 0.0002\text{cm}^{-1}/\text{atm}$ in the A-band are required in order to meet the mission goals of OCO-2 [14]; however, this has not yet been accomplished. It is critical to accurately characterize the pressure-induced shift of an absorption line in order to properly model asymmetric lineshapes accounting for factors such as speed-dependence or line mixing.

A number of previous experimental studies have measured pressure-induced shifts in the oxygen A-band with significant discrepancies. FTS measurements from the late 1990s and early 2000s resulted in measured pressure shift coefficients around two statistically distinct values. Hill et al. [15] and Phillips and Hamilton [16] measured pressure shift coefficients of $\sim 0.01\mathrm{cm}^{-1}/\mathrm{atm}$ while Brown and Plymate [4] and Ritter et al. [17] measured values of $\sim 0.005\mathrm{cm}^{-1}/\mathrm{atm}$. These discrepancies in measurements are further complicated by the fact that Brown and Plymate and Hill determined that pressure shift coefficients for the A-band were independent of the mole fraction of O_2 in N_2, while Phillips and Hamilton and Ritter et al. measured larger shift coefficients for N_2 compared to O_2.

In 2008, two separate studies began to clarify these discrepancies. Predoi-cross [1] measured pressure shifts in agreement with Brown and Plymate and Ritter when spectra were calibrated with CO while results agreed with Hill et al. and Phillips and Hamilton when calibrated with I_2. The discrepancy is explained by one calibration standard providing a more accurate absolute frequency axis. These results demonstrate that a single data set can yield results differing by up to a factor of 2 due to the small errors in the absolute frequency axis arising from uncertainty in the line positions of the calibration molecule. Therefore, an accurately defined frequency axis is extremely important. In the same year, Robichaud et al [9] published a technique for measuring pressure shifts without the need for frequency calibration. They measured relative pressure shifts relying on the precision of the frequency axis provided by frequency stabilized cavity ring-down spectroscopy therefore removing the need for knowledge of the absolute frequency axis. While this approach resulting in measured line position precisions of $\sim$ 1 MHz is appealing, the pressure range of available measurements is limited by the tuning range of the piezo. In addition, these experiments were limited by saturation of stronger lines due to the long effective pathlength, resulting in measured pressure shift for only high-J A-band transitions of pure oxygen.

More recently, Drouin published an extensive lineshape study of the oxygen A-band with the goal of retrieving self-consistent lineshape parameters using multispectrum fitting over a wide range of pressures and temperatures. The study included both cavity ring-down and FTS data. In contrast to the Predoi-Cross work and Robichaud study, this multispectrum approach also found pressure shift coefficients vary with mole fraction of O_2 in N_2. The results from all of these studies will be discussed in more detail in the Section 3.4 and compared to PAS results.

The requirements for accurately measuring pressure-induced shifts, namely, high SNR data over a sufficiently large pressure range with a highly accurate frequency axis make photoacoustic spectroscopy an potentially powerful technique that has not been previously utilized in the oxygen A-band. A newly developed PAS with SNR of $\sim 30,000$ and an absolute frequency uncertainty of 2 MHz, capable of measurements over a wide pressure range (50-4000 Torr) was used to determine pressure shifts coefficients. Accurate characterization is important because the shift parameter in a fit can compensate for asymmetric lineshapes, so these parameters must be well known to fit line mixing and other collisional phenomena. A-band pressure shifts coefficients with lower uncertainties measured with PAS are reported for both oxygen and nitrogen perturbers for both the P and R branches.

3.3 Experimental

The photoacoustic spectrometer is based on a NIST design [18] with several improvements to increase the signal to noise of the data. A schematic of the instrument is displayed in Figure 4.5. An external cavity diode laser (Sacher Lasertechnik ECDL, model TEC520), tunable from 758-770 nm is fiber coupled into a 99:1 PM fiber splitter (Thorlabs, PN780R1A1). The laser frequency is measured with an absolute uncertainty of 2 MHz from the 1% of light directed to a wavemeter (High Finesse, WSU-2) referenced to a frequency stabilized HeNe (Micro-g Lacoste, ML-1) with 100 kHz long-term stability. The remaining 99% of the laser power (~ 20 mW) seeds a tapered amplifier (New Focus, TA-7613) with a free-space output of 800 mW. Two lenses form a Galilean telescope to focus the light on an acousto-optic modulator (Brimrose, TEM 110-25) and the intensity modulated laser beam is collimated and sent through the photoacoustic cell housed in a vacuum chamber.

As described by Gillis[18], the stainless steel photoacoustic cell consists of a 100 mm long, 6mm diameter resonator between a pair of 50 mm long, 30 mm diameter cylindrical baffle chambers. An electret microphone (PUI Audio, POM-5038L-C3310-R) sits at the center of the resonator. Flanges at each end mount wedged 0.5" windows (Thorlabs WW40530-B) used to limit etalon issues. The window seal is formed with flourosilicone o-rings to allow for future measurements at temperatures down to 200K. The cell is enclosed in a vacuum chamber to limit acoustic noise and ambient temperature fluctuations.

The laser modulation frequency is set to excite the lowest order longitudinal mode of the acoustic resonator (1.5-1.6 KHz) in order to maximize the signal to noise of the acquired spectra. The resonant frequency is sensitive to changes pressure, temperature or gas composition, so before each scan, the optical frequency of the laser is tuned to an absorption peak, and the modulation frequency is scanned over a wide range (500Hz-2500 Hz) to properly set the modulation frequency. The measured Q factors vary slightly with pressure, but are typically ~ 20 at ambient pressure.

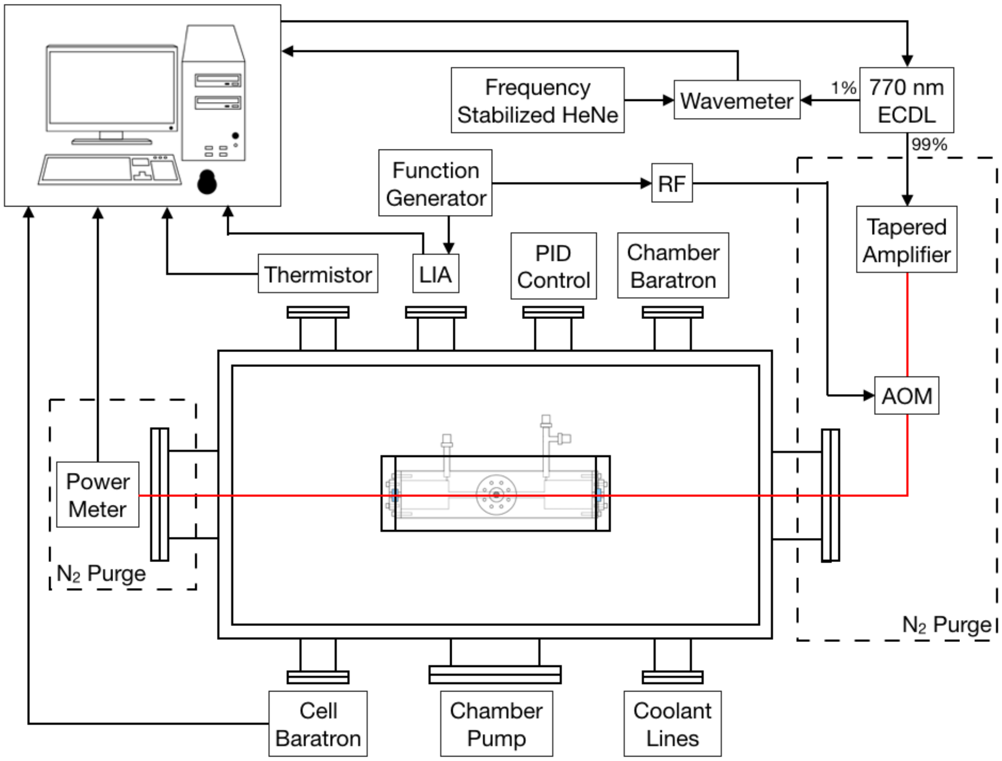

Figure 3.1: Graphic illustration of the PAS experiment

The cell is enclosed in an aluminum housing equipped with 3 custom designed stainless steel/Macor legs mounted to a 12” × 24” optical breadboard to maximize stability and minimize thermal contact with the external environment. This breadboard is placed in a 12” × 12” × 24” custom designed stainless steel vacuum chamber (Kurt J. Lesker Company). The short ends of the chamber are equipped with a 6" Conflat flange which hold 1.5" viewports (Thorlabs VPCH42-B) to allow beam transmission. Each long side has four 2 3/4" Conflat flanges and one 6" Conflat flange. A 1.5" butterfly valve (MDC Vacuum Products 360001) is fixed to one of the 6" Conflat ports to allow for high throughput pump out of the chamber. A 2 3/4" CF flange with two UHV welded 1/4" tubes with VCR connections (Kurt J. Lesker LFT322MVFV) is used for cell gas fill/pumpout lines. A multipin bayonet feedthrough is used to carry the four wire Pt RTD signal and a 2 3/4" CF BNC feedthrough is used for the microphone signal.

The beam exiting the vacuum chamber is directed to a silicon photodetector (Newport 918D-SL-OD3) which measures the peak-to-peak power after the cell. This measured power is corrected for absorption along half of the cell pathlength to normalize the photoacoustic signal to the power at the center of the cell where the microphone is mounted. Two polycarbonate boxes are placed over the beam path both before and after the chamber so that the entire free-space beam path can be purged with nitrogen. A-band absorption by the ambient air along the beam path attenuates the power; however, correcting the power requires knowledge of the lineshape being measured. Therefore, the attenuation problem was minimized to a negligible amount by purging the path with nitrogen.

The cell pressure is monitored with a heated capacitance manometer (MKS 690A) with an uncertainty of 0.08% of the reading up to 10,000 Torr. The temperature was measured with a calibrated Pt RTD with 0.1K uncertainty mounted on the cell in direct contact with the gas sample.

The data acquisition is fully automated so that no intervention is required over the course of a single scan ($\sim$ 20 hours). A full band ($\sim 190cm^{-1}$) scan consists of $\sim 15,000$ data point with 400MHz (0.0133 cm^{-1}) spacing between points. A frequency set point is generated in the custom LabVIEW program, and a PID lock loop based on the wavemeter reading (170 Hz) adjusts parameters to lock the laser frequency to the set point. Fine adjustments are done by tuning the current on the diode while larger corrections are controlled by adjusting the piezo voltage on the cavity of the ECDL. After the standard deviation of the measured wavelength has been <1MHz for 50 consecutive points, the laser is considered locked and data acquisition begins. The pressure and temperature is recorded at every point. In addition the program rapidly alternates between collecting microphone voltages and power meter readings in order to limit the noise introduced by long term power fluctuations. A single point takes approximately 5 seconds, with the stepping and locking of the laser frequency requiring $\sim$ 4 seconds and $\sim$ 1 second averaging time of microphone/power data. In addition, the LabVIEW code corrects for mode hops by adjusting the DC diode current to allow for the broadband, uninterrupted spectra.

The cell and gas lines were heated to $35°C$ and pumped down with a turbo pump for 4 days to reach a base pressure of $\sim\ 2 \times 10^{-5}$ Torr. Efforts were made to limit the amount of water because water efficiently quenches the relaxation mechanism giving rise to the photoacoustic signal. Dry samples were used to minimize both complications in accounting for the response and possible perturbations to the lineshape profiles.

3.4 Results

Pressure shift coefficients were determined for up to J'=28 for the P-branch and J'=30 for the R-branch for both pure oxygen and NIST air samples. Five pressures of pure oxygen data (50-375 Torr) and four pressures of NIST air (100-500 Torr) were included in the data set used to extract pressure shift coefficients. Figure 3.4a displays the photoacoustic spectrum of the 375 Torr sample demonstrating the spectral coverage of the experiments. Higher pressure data was not included because residuals of 500 Torr data showed evidence of line mixing, which can interfere with retrieved pressure shift parameters. There is no evidence of line mixing at the pressures included in the current data set within the signal to noise of the data. The signal to noise of the data declines with pressure and is lower for NIST air compared to oxygen; however all spectra were in the range of 6,000-40,000.

Each pure oxygen spectrum was fit with Nelkin-Ghatak profiles using Labfit[19]. The Voigt profile (VP) resulted in significant W-shaped residuals indicating the need for a narrower profile. Both the speed dependent Voigt (SDVP) and Nelkin-Ghatak profile (NGP) were used. The NGP resulted in residuals with $\sim$ 6 times smaller RMS compared to the SDVP, and $\sim$ 40 times smaller than the VP so all results are from NGP fits; however, it has been shown that the choice of lineshape between SDVP and NGP does not impact the retrieved pressure shift parameter significantly [1]. All initial lineshape parameters were from Drouin 2017 with the exception of the Dicke narrowing parameters taken from Long 2010[2]. The intensities, pressure broadened widths, pressure shift coefficients and narrowing parameters were all floated for each spectrum independently. Figure 3.4b shows the data (dots) and NGP fit profiles (lines) as well as the spectral residuals. All residuals are below 0.1% of the peak absorption value. The total shift observed over the measured pressure range was approximately 80 MHz (difference between teal and pink vertical dashed lines) indicating sufficient sensitivity with the < 0.2 MHz absolute uncertainty in the frequency measurement with precision below 1 MHz.

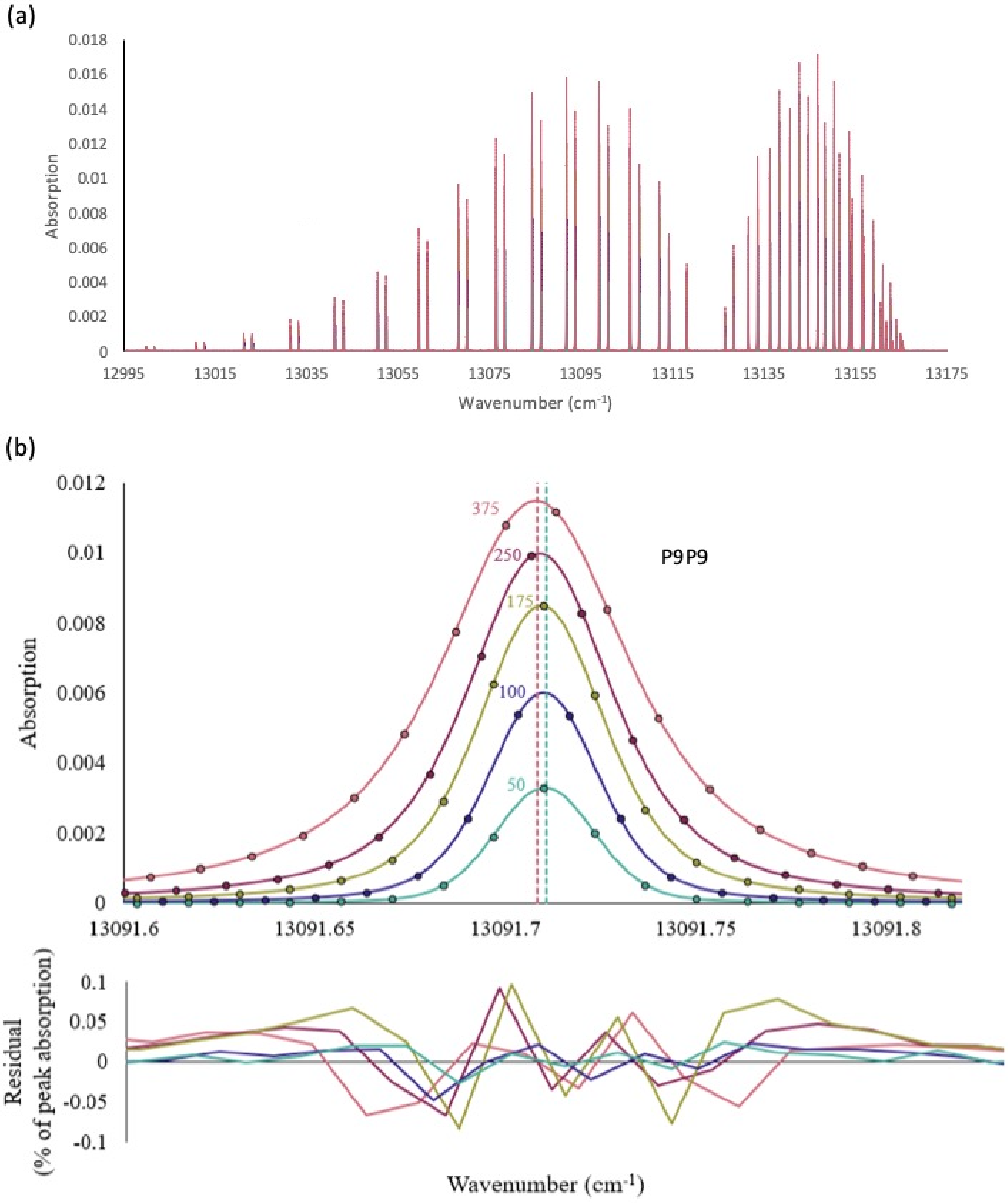

Figure 3.2: (a) Full A-band spectrum of pure oxygen and (b) the P9P9 transition over the range of pure oxygen data recorded fit with Nelkin-Ghatak profiles and the resulting spectral residuals

The results from single spectrum fits were then plotted as a function of pressure. An example of the absolute shift as a function of pressure of P11Q10 is shown in Figure 3.4. A linear function was used to fit the data. Fit uncertainties were typically $0.8 - 3\%$ While the pressure-induced shift values showed significant deviation from previous measurements, the pressure broadened self widths extracted from the photoacoustic data are in good agreement with both Drouin 2017 and Long 2010 and narrowing parameters are in good agreement with Long 2010.

The NIST air data was fit in a similar manner to the oxygen data; however, the oxygen self pressure broadened width coefficients and pressure shift coefficients were fixed to the values determined from the pure oxygen data and the nitrogen pressure broadened width coefficients and pressure shift coefficients were floated. The values for pressure shift coefficients in air were also calculated based on the fit values for oxygen and nitrogen and the composition of the gas sample using a linear combination:

$$\delta_{air} = 0.2072\delta_{O_2} + .7928\delta_{N_2}$$

The results are plotted in Figure 3.4 for oxygen, nitrogen and air pressure shift coefficents as a function of m for the current photoacoustic measurements as well as some previous relevant studies. Error bars indicate 2σ error for all studies. The corresponding values are listed in Table 2.1 where the values in parenthesis show the 2σ error.

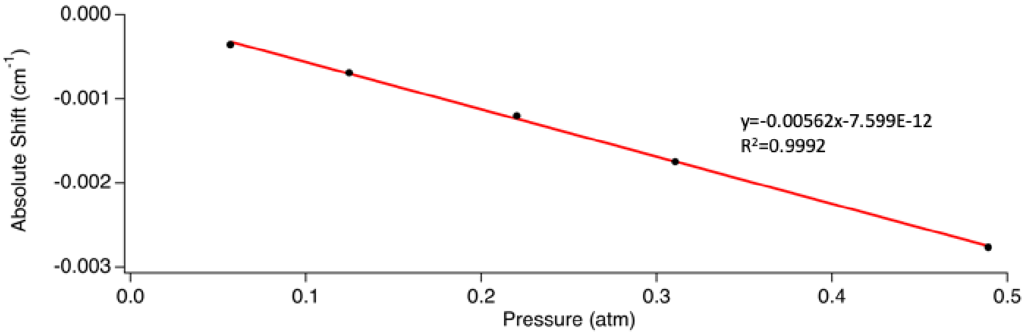

Figure 3.3: Pure oxygen absolute pressure shift (cm^{-1} as a function of pressure (atm) for the P11Q10 transition of the A-band

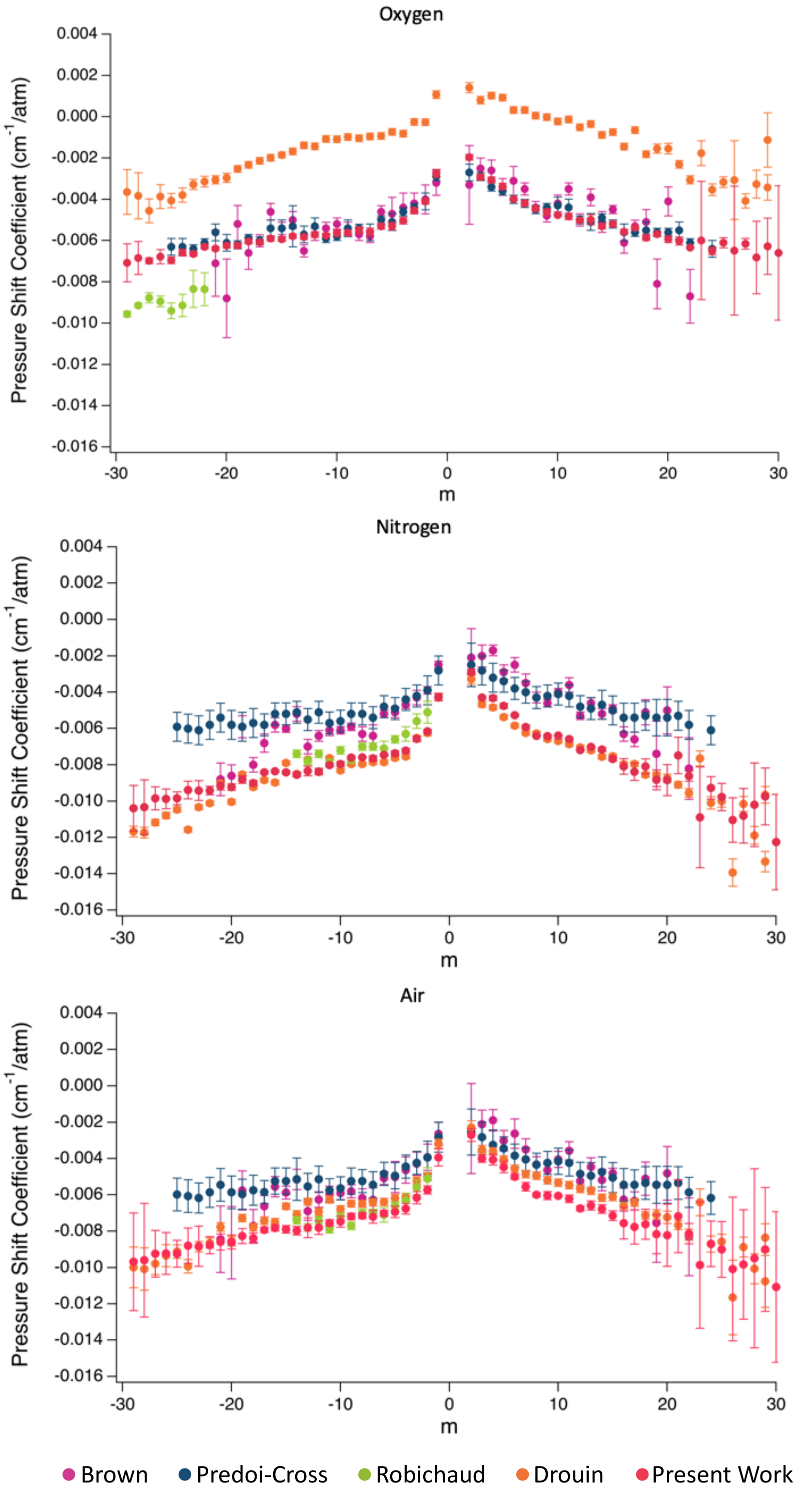

Figure 3.4: Measured pressure-induced shift values for oxygen, nitrogen and air

Table 3.1: Measured O_2 A-Band Pressure-Induced Shift Parameters

Assignment $\Delta N N$”$\Delta J J$”	Position cm^{-1}	δ_{O2} $cm^{-1}atm^{-1}$	δ_{N2} $cm^{-1}atm^{-1}$	δ_{Air} $cm^{-1}atm^{-1}$
P29P29	12999.95707	-0.00708(46)	-0.01039(126)	-0.00969(134)
P29Q28	13001.7097	-0.00684(40)	-0.01033(151)	-0.00959(156)
P27P27	13010.81262	-0.00698(7)	-0.00984(64)	-0.00924(65)
P27Q26	13012.58274	-0.00678(17)	-0.00988(55)	-0.00923(58)
P25P25	13021.29112	-0.00695(8)	-0.00984(36)	-0.00924(37)
P25Q24	13023.07889	-0.00658(8)	-0.00939(48)	-0.00880(49)
P23P23	13031.39436	-0.00664(5)	-0.00941(55)	-0.00883(55)
P23Q22	13033.19994	-0.00630(5)	-0.00942(23)	-0.00877(23)
P21P21	13041.12385	-0.00639(4)	-0.00917(22)	-0.00859(23)
P21Q20	13042.94749	-0.00624(6)	-0.00922(18)	-0.00859(19)
P19P19	13050.48093	-0.00624(5)	-0.00881(20)	-0.00827(21)
P19Q18	13052.32291	-0.00604(5)	-0.00900(13)	-0.00838(14)
P17P17	13059.46667	-0.00608(3)	-0.00841(7)	-0.00792(8)
P17Q16	13061.32742	-0.00590(6)	-0.00835(5)	-0.00783(8)
P15P15	13068.08195	-0.00593(5)	-0.00841(9)	-0.00789(10)
P15Q14	13069.96203	-0.00579(5)	-0.00855(11)	-0.00797(13)
P13P13	13076.32743	-0.00582(6)	-0.00834(27)	-0.00781(27)
P13Q12	13078.22768	-0.00571(7)	-0.00837(17)	-0.00781(18)
P11P11	13084.20355	-0.00575(5)	-0.00801(7)	-0.00754(9)
P11Q10	13086.1253	-0.00562(9)	-0.00796(13)	-0.00747(16)
P9 P9	13091.71056	-0.00563(7)	-0.00760(6)	-0.00719(9)
P9 Q8	13093.65603	-0.00549(8)	-0.00758(1)	-0.00714(8)
P7 P7	13098.84847	-0.00558(9)	-0.00764(15)	-0.00721(17)
P7 Q6	13100.82198	-0.00531(7)	-0.00746(4)	-0.00701(8)
P5 P5	13105.61713	-0.00529(9)	-0.00737(13)	-0.00693(16)
P5 Q4	13107.62872	-0.00504(8)	-0.00722(12)	-0.00676(14)
P3 P3	13112.01614	-0.00454(6)	-0.00657(16)	-0.00615(17)
P3 Q2	13114.10046	-0.00410(6)	-0.00616(9)	-0.00573(11)
P1 P1	13118.04495	-0.00275(10)	-0.00426(21)	-0.00394(10)
R1 R1	13126.39224	-0.00196(7)	-0.00290(166)	-0.00270(167)
R1 Q2	13128.26903	-0.00292(7)	-0.00429(75)	-0.00400(75)

R3 R3	13131.49166	-0.00305(7)	-0.00432(126)	-0.00406(126)
R3 Q4	13133.44123	-0.00338(8)	-0.00476(130)	-0.00447(130)
R5 R5	13136.21726	-0.00399(3)	-0.00527(58)	-0.00500(58)
R5 Q6	13138.205	-0.00419(7)	-0.00592(97)	-0.00555(97)
R7 R7	13140.56756	-0.00445(5)	-0.00640(15)	-0.00599(16)
R7 Q8	13142.58344	-0.00462(8)	-0.00642(74)	-0.00604(75)
R9 R9	13144.54087	-0.00477(2)	-0.00639(20)	-0.00605(20)
R9 Q10	13146.58063	-0.00482(8)	-0.00659(71)	-0.00622(71)
R11R11	13148.1353	-0.00502(5)	-0.00719(38)	-0.00674(38)
R11Q12	13150.19673	-0.00498(12)	-0.00701(33)	-0.00659(35)
R13R13	13151.34876	-0.00531(6)	-0.00716(10)	-0.00677(11)
R13Q14	13153.43057	-0.00520(6)	-0.00767(12)	-0.00715(13)
R15R15	13154.17894	-0.00558(6)	-0.00809(43)	-0.00756(43)
R15Q16	13156.28033	-0.00538(4)	-0.00839(47)	-0.00776(48)
R17R17	13156.62333	-0.00586(7)	-0.00809(41)	-0.00762(42)
R17Q18	13158.74374	-0.00569(4)	-0.00882(54)	-0.00816(54)
R19R19	13158.67919	-0.00593(8)	-0.00883985)	-0.00822(85)
R19Q20	13160.81826	-0.00602(10)	-0.00748(50)	-0.00717(51)
R21R21	13160.34357	-0.00634(2)	-0.00862(14)	-0.00814(14)
R21Q22	13162.50103	-0.00599(143)	-0.01089(288)	-0.00986(322)
R23R23	13161.61331	-0.00650(9)	-0.00927(31)	-0.00869(32)
R23Q24	13163.78896	-0.00611(12)	-0.00977(38)	-0.00900(40)
R25R25	13162.48501	-0.00648(156)	-0.01104(61)	-0.01008(167)
R25Q26	13164.67869	-0.00615(13)	-0.01081(75)	-0.00983(76)
R27R27	13162.95504	-0.00682(88)	-0.01020(115)	-0.00949(145)
R27Q28	13165.16664	-0.00628(68)	-0.00974(78)	-0.00901(104)
R29R29	13163.01953	-0.00660(163)	-0.01225(131)	-0.01107(210)
R29Q30	13165.24897	-0.00617(62)	-0.01723(388)	-0.01491(393)

3.5 Discussion

Table 3.5 summarizes important information for the previous A-band pressure shift studies displayed in Figure 3.4.

The PAS measured oxygen shifts are in good agreement with the previous measurements of Predoi-Cross [1] and Brown [4] although the uncertainties are reduced and there is a smoother J-dependence of the pressure shift coefficient. These values are notably of greater magnitude than the Drouin oxygen values. Although the magnitude is significantly different, the J-dependence follows a similar pattern suggesting an error in the absolute frequency axis calibration lead to the offset observed in the Drouin data.

The PAS measured nitrogen shifts are in good agreement with the Drouin data. To ensure the fits were not constrained to a local minimum due to the initial input values from Drouin, all data was fit a second time with initial guess parameters set to Predoi-Cross values. In this case, the fit results converged to the same values as when Drouin values were used as the initial guess. Again, the errors are smaller than previous studies and a smooth J-dependence is observed.

The PAS air pressure shift coefficients are in good agreement with previous Robichaud measurements. It is likely that the Drouin measurements are artificially high due to the issues with the pure oxygen shifts.

In contrast to many previous studies, results indicate statistically significant difference in values for oxygen and nitrogen shifts. Brown, Predoi-Cross and Robichaud all found comparable values for O_2 and N_2. An earlier study, by Phillips, also found larger shift for nitrogen relative to oxygen, although they found a much larger difference in magnitude. In this case, it was attributed to larger dispersion forces for N_2. The magnitude of the shift can be estimated from the interaction potential which is dominated by dispersion forces for two nonpolar molecules. The shifts are difficult to estimate without more sophisticated calculations so the argument from dispersion forces points out that it is not unreasonable to have larger shifts for nitrogen rather than a strong explanation.

The HITRAN database (cite) tabulates air pressure induced shifts for the oxygen A-band. For the main isotopologue, these values currently correspond to Robichaud measurements in the P-branch and an average of the Predoi-Cross retrieved values of data calibrated to CO and I_2. Due to the sensitivity of the pressure shift coefficients to the absolute frequency axis, and the fact that averaging the Predoi-Cross values is essentially averaging the errors from the two calibration measurements, a need for experimental data with a more reliable frequency axis is required for R-branch shifts. The PAS data provides a new set of measured shifts for the R-branch where previous reliable data is minimal.

Previous O$_2$ A-band Pressure Shift Measurements					
	Method	Pressure Range (Torr)	Absolute Frequency	SNR	$O_2 = N_2$?
Brown	FTS	150-600 (O$_2$) 390-590 (N$_2$)	H_2O, C_2H_2	300	Y
Robichaud	CRDS	1-304* (O$_2$) 1-755* (N$_2$)	-	7,000	Y
Predoi-Cross	FTS	98-337 (O$_2$) 8-3000 (N$_2$)	K and CO	1,000	Y
Drouin	FTS/CRDS	1-1000 (O$_2$) 1-1000 (N$_2$)	K	200/5,000	N
This Work	PAS	50-375 (O$_2$) 100-500 (N$_2$)	Wavemeter	30,000	N

Table 3.3: Summary of previous A-band pressure shift studies

3.6 Conclusion

Pressure shift coefficients were measured for oxygen and air in the oxygen A-band. Photoacoustic spectroscopy provides a number of advantages to reduce the uncertainty in the retrieved parameters. It is the lowest reported uncertainties in the R-branch for oxygen by a factor of 3.

References

[1] Adriana Predoi-Cross et al. "Spectroscopic lineshape study of the self-perturbed oxygen A-band". In: *Journal of Molecular Spectroscopy* 248.2 (Apr. 2008), pp. 85–110. ISSN: 00222852. DOI: `10.1016/j.jms.2007.11.007`.

[2] D. A. Long et al. "O2 A-band line parameters to support atmospheric remote sensing". In: *Journal of Quantitative Spectroscopy and Radiative Transfer* 111.14 (Sept. 1, 2010), pp. 2021–2036. ISSN: 0022-4073. DOI: `10.1016/j.jqsrt.2010.05.011`.

[3] David J. Robichaud et al. "High-accuracy transition frequencies for the O2 A-band". In: *Journal of Molecular Spectroscopy*. Special issue dedicated to the pioneering work of Drs. Edward A. Cohen and Herbert M. Pickett on spectroscopy relevant to the Earth's atmosphere and astrophysics 251.1 (Sept. 1, 2008), pp. 27–37. ISSN: 0022-2852. DOI: `10.1016/j.jms.2007.12.008`.

[4] L.R. Brown and C. Plymate. "Experimental Line Parameters of the Oxygen A Band at 760 nm". In: *Journal of Molecular Spectroscopy* 199.2 (Feb. 2000), pp. 166–179. ISSN: 00222852. DOI: `10.1006/jmsp.1999.8012`.

[5] Brian J. Drouin et al. "Multispectrum analysis of the oxygen A-band". In: *Journal of quantitative spectroscopy & radiative transfer* 186 (Jan. 2017), pp. 118–138. ISSN: 0022-4073. DOI: `10.1016/j.jqsrt.2016.03.037`.

[6] David J. Robichaud et al. "Experimental intensity and lineshape parameters of the oxygen A-band using frequency-stabilized cavity ring-down spectroscopy". In: *Journal of Molecular Spectroscopy* 248.1 (Mar. 2008), pp. 1–13. ISSN: 00222852. DOI: `10.1016/j.jms.2007.10.010`.

[7] D. K. Havey et al. "Ultra-sensitive optical measurements of high-J transitions in the O2 A-band". In: *Chemical Physics Letters* 483.1 (Nov. 24, 2009), pp. 49–54. ISSN: 0009-2614. DOI: `10.1016/j.cplett.2009.10.067`.

[8] Adriana Predoi-Cross et al. "Nitrogen-broadened lineshapes in the oxygen A-band: Experimental results and theoretical calculations". In: *Journal of Molecular Spectroscopy* 251.1 (Sept. 2008), pp. 159–175. ISSN: 00222852. DOI: `10.1016/j.jms.2008.02.010`.

[9] David J. Robichaud et al. "High-precision pressure shifting measurement technique using frequency-stabilized cavity ring-down spectroscopy". In: *Journal of Quantitative Spectroscopy and Radiative Transfer* 109.3 (Feb. 2008), pp. 435–444. ISSN: 00224073. DOI: `10.1016/j.jqsrt.2007.06.005`.

[10] D. A. Long et al. “O2 A-band line parameters to support atmospheric remote sensing. Part II: The rare isotopologues”. In: *Journal of Quantitative Spectroscopy and Radiative Transfer* 112.16 (Nov. 1, 2011), pp. 2527–2541. ISSN: 0022-4073. DOI: `10.1016/j.jqsrt.2011.07.002`.

[11] H. Tran, C. Boulet, and J.-M. Hartmann. “Line mixing and collision-induced absorption by oxygen in the A band: Laboratory measurements, model, and tools for atmospheric spectra computations”. In: *Journal of Geophysical Research: Atmospheres* 111 (D15 2006). ISSN: 2156-2202. DOI: `10.1029/2005JD006869`.

[12] H. Tran and J.-M. Hartmann. “An improved O2 A band absorption model and its consequences for retrievals of photon paths and surface pressures”. In: *Journal of Geophysical Research: Atmospheres* 113 (D18 2008). ISSN: 2156-2202. DOI: `10.1029/2008JD010011`.

[13] D. A. Long, D. J. Robichaud, and J. T. Hodges. “Frequency-stabilized cavity ring-down spectroscopy measurements of line mixing and collision-induced absorption in the O2 A-band”. In: *The Journal of Chemical Physics* 137.1 (July 5, 2012), p. 014307. ISSN: 0021-9606. DOI: `10.1063/1.4731290`.

[14] C. E. Miller et al. “Spectroscopic challenges for high accuracy retrievals of atmospheric CO2 and the Orbiting Carbon Observatory (OCO) experiment”. In: *Comptes Rendus Physique*. Molecular spectroscopy and planetary atmospheres 6.8 (Oct. 1, 2005), pp. 876–887. ISSN: 1631-0705. DOI: `10.1016/j.crhy.2005.09.005`.

[15] Christian Hill, David A. Newnham, and John M. Brown. “Pressure-shift measurements of the oxygen A-band by Fourier-transform spectroscopy”. In: *Journal of Molecular Spectroscopy* 219.1 (May 2003), pp. 65–69. ISSN: 00222852. DOI: `10.1016/S0022-2852(03)00017-1`.

[16] Alexander J. Phillips and Peter A. Hamilton. “Pressure-Shift of the (0,0) and (1,0) Bands of the Oxygen[formula]Transition from Fourier Transform Spectroscopy”. In: *Journal of Molecular Spectroscopy* 174.2 (Dec. 1, 1995), pp. 587–594. ISSN: 0022-2852. DOI: `10.1006/jmsp.1995.0025`.

[17] K. J. Ritter and T. D. Wilkerson. “High-resolution spectroscopy of the oxygen A band”. In: *Journal of Molecular Spectroscopy* 121.1 (Jan. 1, 1987), pp. 1–19. ISSN: 0022-2852. DOI: `10.1016/0022-2852(87)90167-6`.

[18] K. A. Gillis, D. K. Havey, and J. T. Hodges. “Standard photoacoustic spectrometer: Model and validation using O2 A-band spectra”. In: *Review of Scientific Instruments* 81.6 (June 1, 2010), p. 064902. ISSN: 0034-6748. DOI: `10.1063/1.3436660`.

[19] D. Chris Benner et al. “A multispectrum nonlinear least squares fitting technique”. In: *Journal of Quantitative Spectroscopy and Radiative Transfer* 53.6 (June 1, 1995), pp. 705–721. ISSN: 0022-4073. DOI: `10.1016/0022-4073(95)00015-D`.

Chapter 4

LINE MIXING AND COLLISION-INDUCED ABSORPTION IN THE OXYGEN A-BAND

4.1 Abstract

Accurate characterization of line mixing and collision-induced absorption in the oxygen A-band is critical for high-resolution atmospheric composition measurements. Specifically, improper modeling of line mixing and collision-induced absorption are currently believed to be the largest spectroscopic uncertainties impacted the retrieved dry air mole fraction of CO_2 for the OCO missions. We present the first use of photoacoustic spectroscopy to measure line mixing and collision-induced absorption in the oxygen A-band.

4.2 Introduction

The oxygen A-band is used in a number of atmospheric composition measurements due to the uniform well known concentration of oxygen throughout the atmosphere. Line mixing and collision-induced absorption are collisional effects which impact the spectra in the far wings and baseline. Many of the atmospheric A-band measurements involve long path lengths and high optical densities making these measurements very sensitive to wing and baseline absorption. These phenomena result in relatively small, yet significant perturbations to spectra that need to be accounted for. Therefore, there is a need for accurate laboratory measurements.

A typical OCO-2 satellite A-band spectrum and the spectral residuals are shown in Figure 4.1. Almost the whole R-branch and much of the low-J P-branch is saturated making the retrievals most sensitive to the areas between absorption lines. The residuals show structured peaks on the order of 1% which occur between the lines of a doublet. This type of residual is typical of improperly characterized line mixing. Because the line mixing and collision-induced absorption both impact the wings and baseline of spectra, errors is capturing the physics of one phenomena can result in errors in the other from fitting. Therefore, high SNR data over a wide range of pressures is required to constrain line mixing and collision-induced absorption to pressure dependencies so accurate physics can be captured in the models. This is critical to the OCO missions because errors in the oxygen spectroscopy propagate through to errors in the retrieved carbon dioxide concentrations.

Due to the difficulty in measuring these phenomena, in the past, high pressure Fourier transform spectroscopy has been used at pressures well above atmospherically relevant pressures in order to exaggerate these effects to characterize them, or cavity ring-down spectroscopy has been used to utilize the long effective pathlength making the technique sensitive to the weak baseline absorption.

Tran and Hartmann [1, 2] measured oxygen and air spectra at very high pressures (20-200 atm) with Fourier Transform spectroscopy. At these pressures, the spectra are also largely saturated with strong signals from the wings of peaks. This study also incorporated atmospheric spectra. The resonant lineshapes were fit with a full relaxation matrix model for line mixing. This model was then subtracted from the data and any "leftover" absorption is attributed to collision-induced absorption. This was the first high-resolution laboratory study of line mixing and collision-induced absorption in A-band resulting in valuable information for

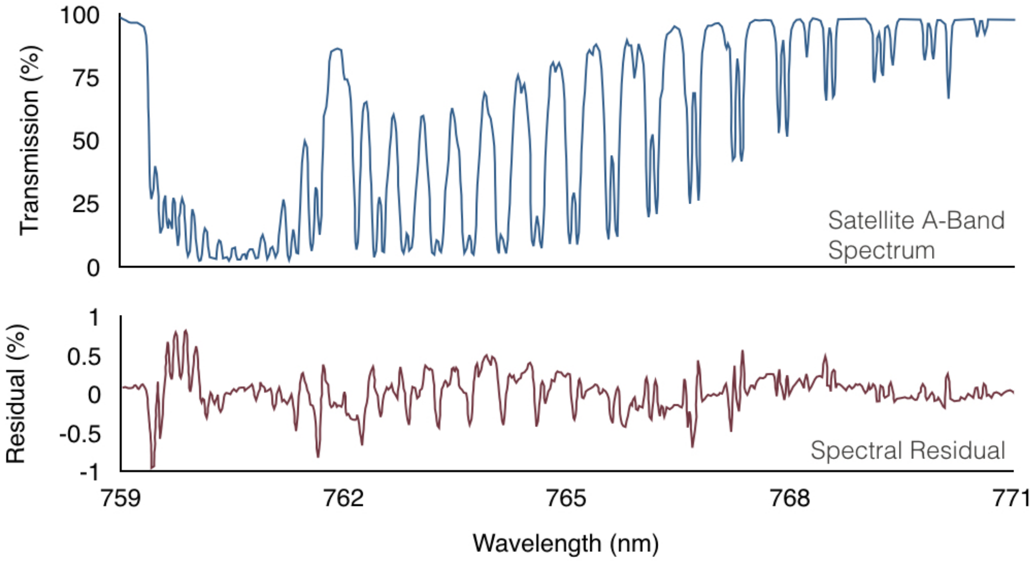

Figure 4.1: A-band satellite spectrum and residual

atmospheric composition measurements.

Cavity ring-down spectroscopy has been used to measure line mixing and collision-induced absorption in the A-band by Spiering [3, 4, 5] and Long[6] for the p-branch only. Both studies attempt to model resonant lines and line mixing and attribute the smooth remaining absorption to collision-induced absorption. However, it is difficult to fully capture the line mixing with saturated spectra and any additional or deficient modeled absorption due to errors in line mixing modeling, is manifested as deficient or extra absorption in the collision-induced absorption profile.

While these measurements provide valuable insight into the line mixing and collision-induced absorption in the oxygen A-band, there are limitations of each technique. The Fourier transform spectroscopy data must be background corrected. Minor errors in this process could lead to large errors in the retrieved collision-induced absorption profile due to the extremely weak nature of the feature relative to the resonant lines. The long effective pathlength of cavity ring-down spectroscopy provides high sensitivity measurements; however, even at moderate pressures, the spectra are saturated. Having only wing information makes decoupling line mixing and collision-induced absorption measurements more complicated without the additional constraints provided by the line core information. Drouin attempted to leverage the advantages of each technique by fitting line mixing and extracting collision-induced absorption profiles for both oxygen and air using a multispectrum fitting approach which included Fourier transform spectroscopy and cavity ring-down data [7]. The retrieved collision induced absorption profiles were much narrower than those previously measured. The results from Drouin 2017 will be discussed further and compared with the data from this work in Section 4.7.

In addition to the experimental efforts to model line mixing and collision-induced absorption in the oxygen A-band, some recent theoretical calculations of line shapes for the collision induced absorption profiles have been published. [8, 9, 10]. These lineshapes provide a potential model to constrain collision-induced absorption to rather than simply looking at what is leftover after all other parameters have been fit. This recent theoretical work will be discussed further in Section 4.7.

In this work we present new data taken with photoacoustic spectroscopy which has not previously been utilized for oxygen A-band line mixing or collision-induced absorption measurements. Photoacoustic spectroscopy has many advantages including it is a zero background technique, with a large dynamic range and high sensitivity. The zero-background nature of PAS allows for accurate measurements of weak baseline effects like collision-induced absorption without introducing additional error from background subtractions. They large dynamic range also allows for the measurement of unsaturated lineshapes over a wide pressure range (up to 4,000 Torr in this case) which allows for additional constraints in the line mixing models where intensity is exchanged between the peaks and wings of absorption lines. Finally, the high SNR of the data is useful for measuring line mixing and collision-induced absorption, because these small, weak effects can be observed in the laboratory setting.

4.3 Line Mixing

When the spacing between optical transitions of the same isotopologue of the same species is the same order of magnitude as the pressure broadened width, collisional population exchange can result in intensity exchange between individual absorption lines known as line mixing. A collision between two molecules can result in population transfer followed by photon absorption and a second collisional transfer. In this case, the initial and final states of the molecules are unchanged, but the energy of the absorbed photon differs. This results in an intensity exchange between the absorption lines and is summarized graphically in Figure 4.2. Due to detail balance relationships, there is a net transfer from stronger lines to weaker ones impacting the wings and peaks of lines most significantly. Line mixing increases at higher pressure due to the collisional nature of the effect. The current data set shows line mixing effects in the residuals at pressures as low as 500 Torr for pure oxygen.

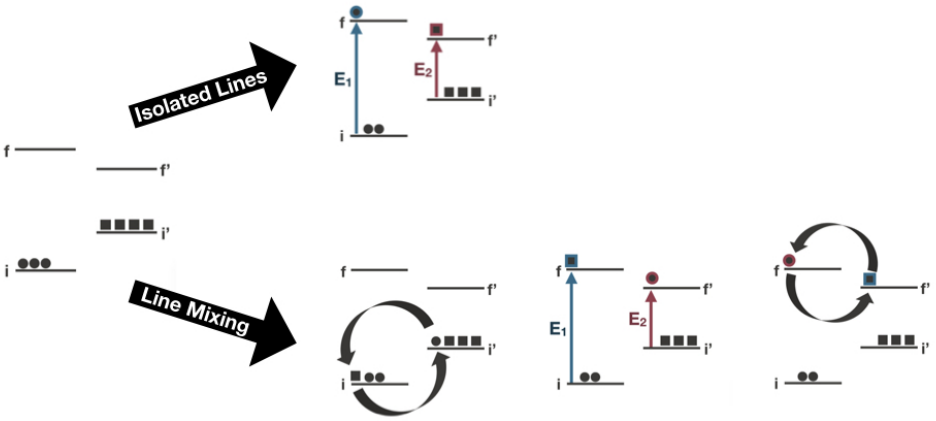

Figure 4.2: Line mixing mechanism

4.4 Collision-Induced Absorption

In addition to the resonant absorption which is proportional to the number density and square of the dipole moment, collisionally induced dipoles can lead to additional absorption. While line mixing results in an intensity exchange between individual absorption lines, the integrated area of the entire band remains constant. On the other hand, collision-induced absorption is addition absorption apearing as a weak continuum feature under the resonant absorption line and scales with number density squared due to the bimolecular nature of the collision. These collisions are very short lived, on the order of 10^{-13} s, leading to a broad absorption feature under the resonant absorption. In the A-band, the collision-induced absorption is very weak compared to the resonant lines. Recently, theoretical studies of collision-induced absorption in the oxygen A-band have suggested that the shape of the feature is impacted by the identity of the perturber [11]. These calculated collision-induced absorption lineshapes may provide reasonable basis functions to constrain measured collision-induced absorption.

4.5 Experimental

The photoacoustic spectrometer is based on a NIST design [12] with several improvements to increase the signal to noise of the data. A schematic of the instrument is displayed in Figure 4.5. An external cavity diode laser (Sacher Lasertechnik ECDL, model TEC520), tunable from 758-770 nm is fiber coupled into a 99:1 PM fiber splitter (Thorlabs, PN780R1A1). The laser frequency is measured with an absolute uncertainty of 2 MHz from the 1% of light directed to a wavemeter (High Finesse, WSU-2) referenced to a frequency stabilized HeNe (Micro-g Lacoste, ML-1) with 100 kHz longterm stability. The remaining 99% of the laser power (~ 20 mW) seeds a tapered amplifier (New Focus, TA-7613) with a free-space output of 800 mW. Two lenses form a Galilean telescope to focus the light on an acousto-optic modulator (Brimrose, TEM 110-25) and the intensity modulated laser beam is collimated and sent through the photoacoustic cell housed in a vacuum chamber.

As described by Gillis[12], the stainless steel photoacoustic cell consists of a 100 mm long, 6mm diameter resonator between a pair of 50 mm long, 30 mm diameter cylindrical baffle chambers. An electret microphone (PUI Audio, POM-5038L-C3310-R) sits at the center of the resonator. Flanges at each end mount wedged 0.5" windows (Thorlabs WW40530-B) used to limit etalon issues. The window seal is formed with flourosilicone o-rings to allow for future measurements at temperatures down to 200K. The cell is enclosed in a vacuum chamber to limit acoustic noise and ambient temperature fluctuations.

The laser modulation frequency is set to excite the lowest order longitudinal mode of the acoustic resonator (1.5-1.6 KHz) in order to maximize the signal to noise of the acquired spectra. The resonant frequency is sensitive to changes pressure, temperature or gas composition, so before each scan, the optical frequency of the laser is tuned to an absorption peak, and the modulation frequency is scanned over a wide range (500Hz-2500 Hz) to properly set the modulation frequency. The measured Q factors vary slightly with pressure, but are typically ~ 20 at ambient pressure.

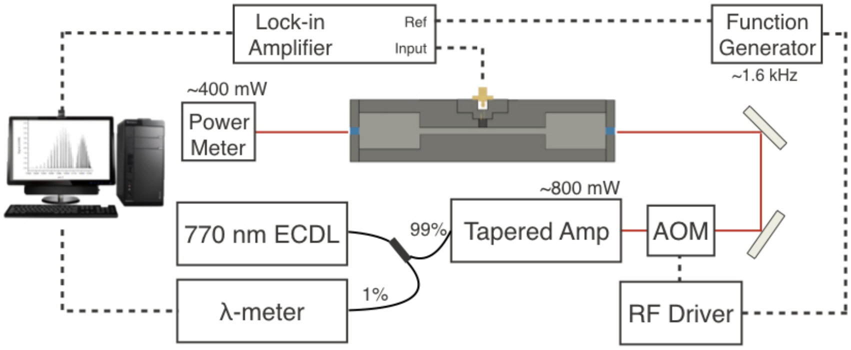

Figure 4.3: Graphic illustration of the PAS experiment

The cell is enclosed in an aluminum housing equipped with 3 custom designed stainless steel/Macor legs mounted to a 12” × 24” optical breadboard to maximize stability and minimize thermal contact with the external environment. This breadboard is placed in a 12” × 12” × 24” custom designed stainless steel vacuum chamber (Kurt J. Lesker Company). The short ends of the chamber are equipped with a 6" Conflat flange which hold 1.5" viewports (Thorlabs VPCH42-B) to allow beam transmission. Each long side has four 2 3/4" Conflat flanges and one 6" Conflat flange. A 1.5" butterfly valve (MDC Vacuum Products 360001) is fixed to one of the 6" Conflat ports to allow for high throughput pump out of the chamber. A 2 3/4" CF flange with two UHV welded 1/4" tubes with VCR connections (Kurt J. Lesker LFT322MVFV) is used for cell gas fill/pumpout lines. A multipin bayonet feedthrough is used to carry the four wire Pt RTD signal and a 2 3/4" CF BNC feedthrough is used for the microphone signal.

The beam exiting the vacuum chamber is directed to a silicon photodetector (Newport 918D-SL-OD3) which measures the peak-to-peak power after the cell. This measured power is corrected for absorption along half of the cell pathlength to normalize the photoacoustic signal to the power at the center of the cell where the microphone is mounted. Two polycarbonate boxes are placed over the beam path both before and after the chamber so that the entire free-space beam path can be purged with nitrogen. A-band absorption by the ambient air along the beam path attenuates the power; however, correcting the power requires knowledge of the lineshape being measured. Therefore, the attenuation problem was minimized to a negligible amount by purging the path with nitrogen.

The cell pressure is monitored with a heated capacitance manometer (MKS 690A) with an uncertainty of 0.08% of the reading up to 10,000 Torr. The temperature was measured with a calibrated Pt RTD with 0.1K uncertainty mounted on the cell in direct contact with the gas sample.

The data acquisition is fully automated so that no intervention is required over the course of a single scan ($\sim$ 20 hours). A full band ($\sim 190cm^{-1}$) scan consists of $\sim 15,000$ data point with 400MHz (0.0133 cm^{-1}) spacing between points. A frequency set point is generated in the custom LabVIEW program, and a PID lock loop based on the wavemeter reading (170 Hz) adjusts parameters to lock the laser frequency to the set point. Fine adjustments are done by tuning the current on the diode while larger corrections are controlled by adjusting the piezo voltage on the cavity of the ECDL. After the standard deviation of the measured wavelength has been <1MHz for 50 consecutive points, the laser is considered locked and data acquisition begins. The pressure and temperature is recorded at every point. In addition the program rapidly alternates between collecting microphone voltages and power meter readings in order to limit the noise introduced by long term power fluctuations. A single point takes approximately 5 seconds, with the stepping and locking of the laser frequency requiring $\sim$ 4 seconds and $\sim$ 1 second averaging time of microphone/power data. In addition, the LabVIEW code corrects for mode hops by adjusting the DC diode current to allow for the broadband, uninterrupted spectra.

The cell and gas lines were heated to $35°C$ and pumped down with a turbo pump for 4 days to reach a base pressure of $\sim\ 2 \times 10^{-5}$ Torr. Efforts were made to limit the amount of water because water efficiently quenches the relaxation mechanism giving rise to the photoacoustic signal. Dry samples were used to minimize both complications in accounting for the response and possible perturbations to the lineshape profiles.

4.6 Results and Discussion

All spectra were fit using Labfit [13] as single spectrum fits for each pressure. The full relaxation matrix with a scaling factor was used for line mixing. Collision-induced absorption profiles result from left over absorption.

Figure 4.4 shows a 500 Torr pure oxygen doublet fit with numerous lineshapes with and without line mixing. It is clear that the SDNGP is required to accurately capture the lineshape within the signal to noise of the data. Other lineshapes show systematic residuals in which pressure-induced shifts, and narrowing parameters attempt to account for what is truly line mixing.

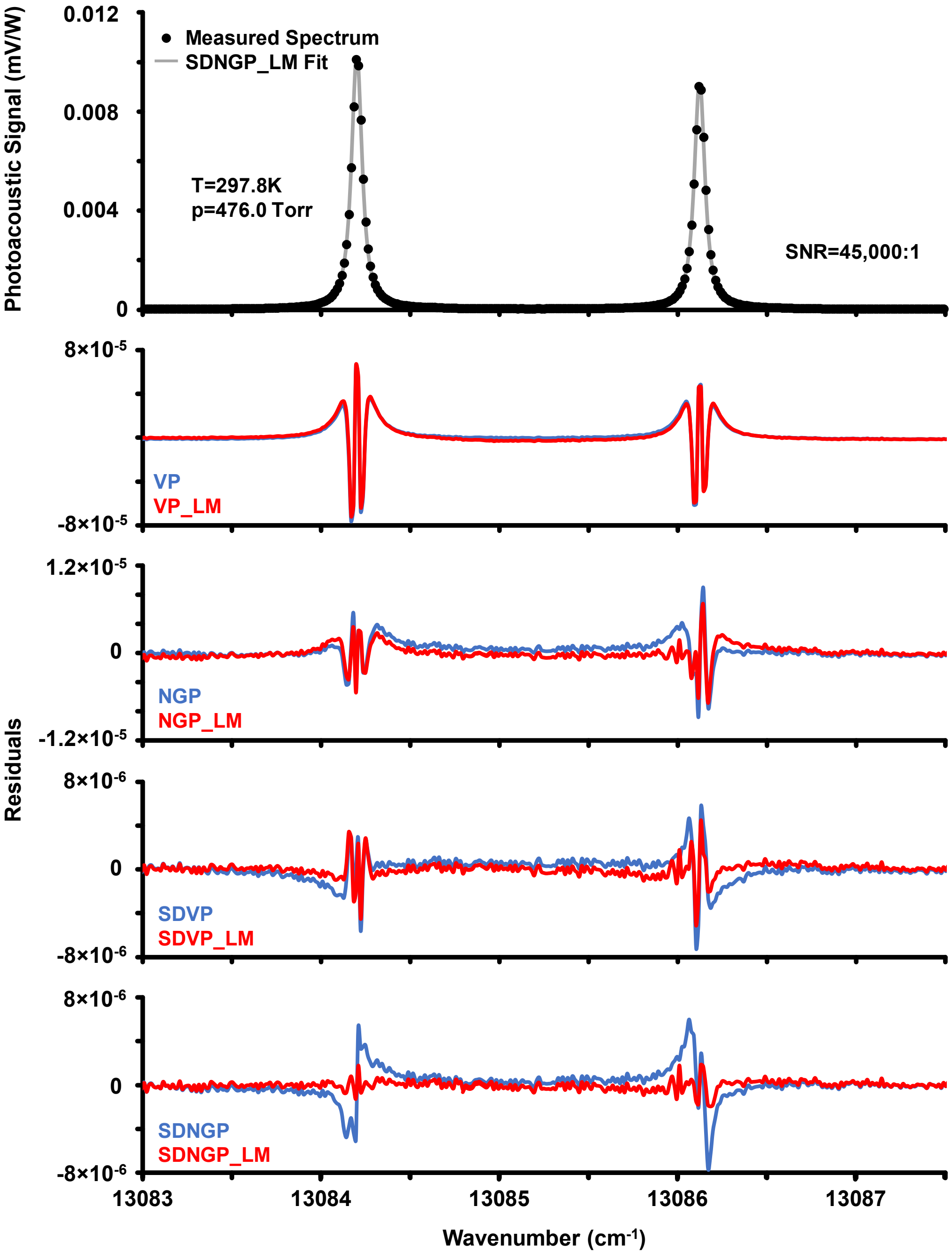
Photoacoustic Signal (mV/W)
0.012
0.008
0.004
0
Measured Spectrum
SDNGP_LM Fit
T=297.8K
p=476.0 Torr
SNR=45,000:1
8×10-5
-8×10-5
VP
VP_LM
1.2×10-5
0
-1.2×10-5
NGP
NGP_LM
Residuals
8×10-6
0
-8×10-6
SDVP
SDVP_LM
8×10-6
0
-8×10-6
SDNGP
SDNGP_LM
13083
13084
13085
13086
13087
Wavenumber (cm-1)

Figure 4.5 shows the 1500 Torr data with the LM mixing model currently used by OCO-2. The model in use is the scaled full relaxation matrix from Tran and Hartmann [2] where = 2 off-diagonal matrix elements are scales by -0.5 and all other elements are set to 0. The bottom panel shows the spectrum fit in segments where the line mixing coefficients are adjusted separately for each segment. In addition, the = 1 elements are also scaled in addition to the = 2 approach by Drouin. This approach clearly results in a smoother, more physical leftover absorption profile to be attributed to collision-induced absorption. Notably, the current data has sufficient signal to noise to see the "spikes" between lines of a doublet that are observed in the satellite spectra for the first time in a laboratory setting. The reduction of the spikes between the lines of a doublet are most strongly impacted by the inclusion of = 1 line mixing in the fits. Adjusting the line mixing parameters independently across the bad severely minimizes the residuals on the absorption lines. It is likely that the residuals on line centers are partially due to improper resonant lineshape. Labfit was limited to Nelkin-Ghatak profile or speed-dependent Voigt profile, and speed-dependent Voigt was chosen as better fits resulted; however, 4.4 shows that the speed-dependent Nelkin-Ghatak profile is required to fit the data.

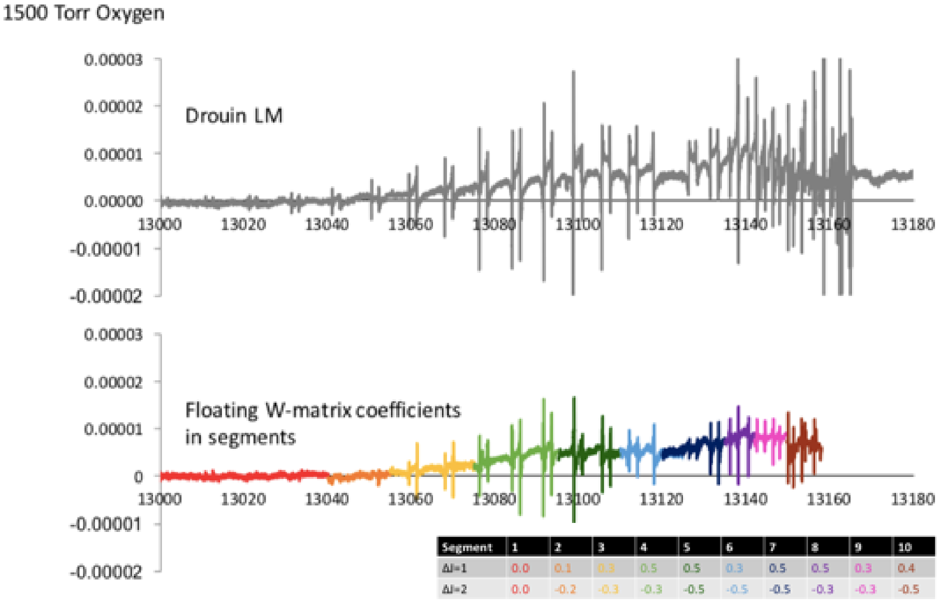

Segment	1	2	3	4	5	6	7	8	9	10
ΔJ=1	0.0	0.1	0.3	0.5	0.5	0.3	0.5	0.5	0.3	0.4
ΔJ=2	0.0	-0.2	-0.3	-0.3	-0.5	-0.5	-0.5	-0.3	-0.3	-0.5

Figure 4.5: Line mixing treatment

Figure 4.6 shows the CIA profiles determined from leftover absorption after fitting resonant lines and line mixing at a number of pressures normalized to number density squared. If these profiles were truly due to collision-induced absorption, they should fall on top of one another on this plot. While the two highest pressures agree exceptionally well, the lower pressures deviate from the number density squared dependence. This is likely due to errors in characterizing line mixing.

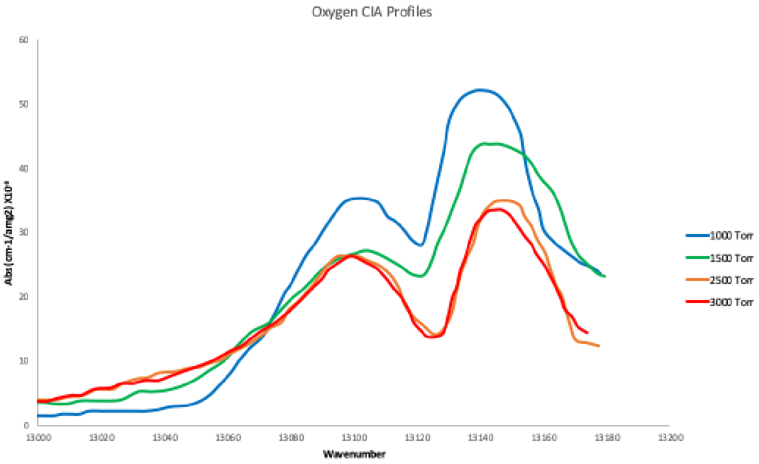

Figure 4.6: CIA profiles for different pressures

Figure 4.7 shows the highest pressure collision-induced absorption profiles compared to previous results. The P-branch agrees well with Tran and Hartmann, but the R-branch is in better agreement with Drouin. The deviation is like due to line mixing treatment. The resulting collision-induced absorption profile is expected to be least impacted by line mixing treatment in the P-branch where lines are further spaced and most sensitive to line mixing treatment at the bandhead. The retrieved profiles cannot be fit with a linear combination of the theoretically calculated profiles mainly due to the deep dip between branches. This area is known to be very sensitive to intrabranch line mixing.

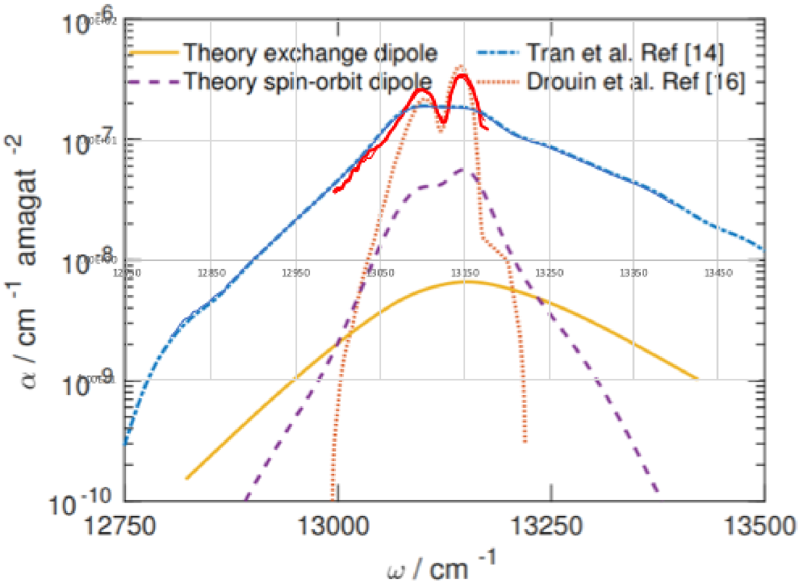

Figure 4.7: CIA comparison

4.7 Conclusion

Photoacoustic spectroscopy was used to measure oxygen and air in the A-band region to characterize line mixing and collision-induced absorption. The high signal to noise data provides new insight into adjustments required to the line mixing model and the resulting collision-induced absorption.

BIBLIOGRAPHY

[1] H. Tran, C. Boulet, and J.-M. Hartmann. “Line mixing and collision-induced absorption by oxygen in the A band: Laboratory measurements, model, and tools for atmospheric spectra computations”. In: *Journal of Geophysical Research: Atmospheres* 111 (D15 2006). ISSN: 2156-2202. DOI: `10.1029/2005JD006869`.

[2] H. Tran and J.-M. Hartmann. “An improved O2 A band absorption model and its consequences for retrievals of photon paths and surface pressures”. In: *Journal of Geophysical Research: Atmospheres* 113 (D18 2008). ISSN: 2156-2202. DOI: `10.1029/2008JD010011`.

[3] Frans R. Spiering et al. “Collision-induced absorption in the O2 B-band region near 670 nm”. In: *Physical Chemistry Chemical Physics* 13.20 (May 3, 2011), pp. 9616–9621. ISSN: 1463-9084. DOI: `10.1039/C1CP20403C`.

[4] Frans R. Spiering and Wim J. van der Zande. “Collision induced absorption in the a1(v = 2) X3g(-)(v = 0) band of molecular oxygen”. In: *Physical chemistry chemical physics: PCCP* 14.28 (July 28, 2012), pp. 9923–9928. ISSN: 1463-9084. DOI: `10.1039/c2cp40961e`.

[5] Frans R. Spiering et al. “Line mixing and collision induced absorption in the oxygen A-band using cavity ring-down spectroscopy”. In: *The Journal of Chemical Physics* 133.11 (Sept. 21, 2010), p. 114305. ISSN: 0021-9606. DOI: `10.1063/1.3460924`.

[6] D. A. Long, D. J. Robichaud, and J. T. Hodges. “Frequency-stabilized cavity ring-down spectroscopy measurements of line mixing and collision-induced absorption in the O2 A-band”. In: *The Journal of Chemical Physics* 137.1 (July 5, 2012), p. 014307. ISSN: 0021-9606. DOI: `10.1063/1.4731290`.

[7] Brian J. Drouin et al. “Multispectrum analysis of the oxygen A-band”. In: *Journal of quantitative spectroscopy & radiative transfer* 186 (Jan. 2017), pp. 118–138. ISSN: 0022-4073. DOI: `10.1016/j.jqsrt.2016.03.037`.

[8] Tijs Karman, Ad van der Avoird, and Gerrit C. Groenenboom. “Line-shape theory of the X3ga1g,b1g+ transitions in O2–O2 collision-induced absorption”. In: *The Journal of Chemical Physics* 147.8 (Aug. 28, 2017), p. 084307. ISSN: 0021-9606. DOI: `10.1063/1.4990662`.

[9] Tijs Karman et al. “O2O2 and O2N2 collision-induced absorption mechanisms unravelled”. In: *Nature Chemistry* 10.5 (May 2018), pp. 549–554. ISSN: 1755-4330, 1755-4349. DOI: `10.1038/s41557-018-0015-x`.

[10] Tijs Karman, Ad van der Avoird, and Gerrit C. Groenenboom. “Potential energy and dipole moment surfaces of the triplet states of the O2(X3g) O2(X3g,a1g,b1g+) complex”. In: *The Journal of Chemical Physics* 147.8 (Aug. 28, 2017), p. 084306. ISSN: 0021-9606. DOI: `10.1063/1.4990661`.

[11] Tijs Karman et al. “O2O2 and O2N2 collision-induced absorption mechanisms unravelled”. In: *Nature Chemistry* 10.5 (May 2018), pp. 549–554. ISSN: 1755-4330, 1755-4349. DOI: `10.1038/s41557-018-0015-x`.

[12] K. A. Gillis, D. K. Havey, and J. T. Hodges. “Standard photoacoustic spectrometer: Model and validation using O2 A-band spectra”. In: *Review of Scientific Instruments* 81.6 (June 1, 2010), p. 064902. ISSN: 0034-6748. DOI: `10.1063/1.3436660`.

[13] D. Chris Benner et al. “A multispectrum nonlinear least squares fitting technique”. In: *Journal of Quantitative Spectroscopy and Radiative Transfer* 53.6 (June 1, 1995), pp. 705–721. ISSN: 0022-4073. DOI: `10.1016/0022-4073(95)00015-D`.